UCL Université catholique de Louvain

École polytechnique de Louvain (EPL)

Fabrication and characterization of mats made of soft LbL nanotubes

Dissertation presented by
Céline VLEMINCQ

for obtaining the Master's degree in
Chemical and Materials Engineering

Supervisor(s)
Sophie DEMOUSTIER, Alain JONAS

Reader(s)
Etienne FERAIN, Charles-André FUSTIN

Academic year 2015-2016

Abstract

In natural tissues, nanofibrillar networks have an important role as support, to control crystallization processes or guide motion, mostly due to both their structure and the numerous possible chemical interactions of their building elements. These observations have inspired the development of mats of nanofibers or nanotubes incorporating synthetic materials and numerous functional macromolecules. In the present work, a new method is proposed to obtain mats of nanotubes based on, first, the production of nanotubes by combining the membrane-templated strategy and layer-by-layer (LbL) adsorption and, subsequently, the filtration and sedimentation of the nanotubes over a substrate. In this context, the main objective of this work is to investigate the building process of mats from the nanotubes and its control parameters by characterizing the morphology and the physical properties (Young's modulus) of the mats as a function of some varying parameters (number of bilayers of the nanotubes, degree of humidity, quantity of nanotubes, diameter of the nanotubes). This study is performed for nanotubes made of poly(sodium 4-styrenesulfonate) (PSS) and poly(allylamine hydrochloride) (PAH) polyelectrolytes with also a brief investigation of the PAH and poly(acrylic acid) (PAA) combination. We show that mats of well-defined nanotubes can be obtained provided proper conditions are used, and that it is possible to stack mats made of different nanotubes to obtain more complex systems. First measurements of the Young's modulus of the mats provide values of ca. 100 MPa, close to what is expected for multilayers made of the same polyelectrolytes.

Remerciements

Je tiens tout d'abord à remercier mes promoteurs, Sophie Demoustier et Alain Jonas, mais également Karine Glinel pour m'avoir offert l'opportunité de travailler sur ce sujet, pour leur très grande disponibilité et leurs conseils avisés.

Je souhaite également remercier mes assistants, Delphine Magnin et Shouwei Zhang, pour m'avoir aidé dans la réalisation de mes expériences et pour les nombreuses discussions constructives.

Je remercie également toute l'équipe du pôle BSMA pour leur accueil et leur grande disponibilité. Un merci tout particulier à Cécile D'Haese et Bernard Nysten pour leur aide en AFM, à Etienne Ferain pour la mise à disposition de membranes de polycarbonate et la réalisation d'essais de porométrie, à Claude Poleunis pour la réalisation d'essais ToF-SIMS, à Catherine Philippart pour ma formation en épifluorescence et les nombreux conseils, à Varvara Gribova pour la réalisation d'essais en microscopie confocale, à Colette Douchamps pour ma formation SEM et à Pascale Lipnik pour les coupes au microtome et l'aide en microscopie optique.

Merci également à mes amis pour m'avoir soutenue lors de la réalisation et la rédaction de ce travail.

Et enfin, merci à mes parents, ma sœur et Julien pour leurs encouragements et leur soutien au quotidien.

Contents

List of abbreviations

AFM	Atomic Force Microscopy
CLSM	Confocal Laser Scanning Microscopy
EDC	1-Ethyl-3-(3-dimethylaminopropyl)carbodiimide
FITC	Fluorescein isothiocyanate
LbL	Layer-by-Layer
L_p	Persistence length
PAH	Poly(allylamine hydrochloride)
PC	Polycarbonate
PEM	Polyelectrolyte multilayer
PET	Polyethylene terephthalate
PSS	Poly(sodium 4-styrenesulfonate)
R_{EE}	RMS average end-to-end distance
RITC	Rhodamine isothiocyanate
SEM	Scanning Electron Microscopy
Sulfo-NHS	N-hydroxy sulfosuccinimide sodium salt
ToF-SIMS	Time of Flight - Secondary Ion Mass Spectrometry

Chapter 1

Introduction

Many natural tissues are composed of nanofibrillar networks. An obvious example is the collagen fiber network of the extracellular matrix. The role of this network is to provide structural support, shape and strength for tissues. Another example is the supramolecular fibrillar scaffold of collagen fibrils in bones which provides a guide for the biomineralization. Therefore these networks of nanofibers have an important role in nature and offer support, control of crystallization processes, strengthening of a tissue, etc. thanks to their structure and the numerous possible chemical interactions of their building elements.[1] So researchers are trying to develop methods to design, in a controlled way, such structures incorporating numerous functional macromolecules and synthetic materials. A possible approach to do that is to produce nanotubes, with various building elements, which are then filtrated to form a mat. The use of nanotubes in the mat presents several advantages. They possess a large specific surface area which is attractive for catalysis. And they also have interior and exterior surfaces that can be separately functionalized.

To produce nanotubes, there are two categories of approaches: self-assembly or the use of templates. Self assembly method is for example efficient to produce carbon, boron nitride or polypeptide nanotubes but the range of building blocks is very restricted. The use of a template can be done in two ways. The template can be nanofibers processed by electrospinning on which a deposition method is performed, such as chemical or physical vapor deposition, spincoating or spraying. The template will be subsequently removed by thermal decomposition or a selective solvent. However all materials are not adapted to these deposition methods. In another way, nanotubes can be produced from a deposition method in a nanoporous template which will also be removed. A possible deposition method is the polymerization but again this method imposes restrictions to the building elements. Another method is by wetting, i.e., the polymer material is placed as a powder or pellets on the top of the nanoporous template and then the system is heated so that the polymer flows along the pore walls. A precise control of the nanotube dimensions is more difficult.[2] A last proposed deposition method is the layer-by-layer (LbL) adsorption which consists of alternate adsorption of complementary species such as oppositely charged polyelectrolytes. This approach, combined with the template method, offers a large range of possible building elements and a great control over the nanotube dimensions. It is for these reasons that we selected this technique to produce nanotubes.

The LbL method combined with a template has already been extensively studied as will be explained in the next section. By contrast the process to produce mats from these nanotubes and its control parameters is very new and still not well understood. In this context, the main objective of this study is thus to investigate the build-up process by characterizing the morphology and the physical properties (Young's modulus) of the mats as a function of some varying parameters (number of bilayers of the nanotubes, degree of humidity, quantity of nanotubes, diameter of the nanotubes). In this study we chose to focus on nanotubes made of one strong polyelectrolyte, poly(sodium 4-styrenesulfonate) (PSS), and one weak polyelectrolyte, poly(allylamine hydrochloride) (PAH) since LbL with this system has already been deeply studied.[3]

This report is divided into four chapters. The first chapter summarizes all the information obtained from the literature. It aims at overviewing the LbL technique and the membrane-templated strategy. Then general concepts of polyelectrolyte adsorption and multilayer build-up are introduced. And the influence of some processing parameters on the multilayer build-up and the effect of some external conditions are presented for a flat substrate and in nanopores when the information was available. The second chapter is the experimental section and presents the methods for the production and the characterization of the nanotubes and the mats. The third chapter introduces the results and the discussion and is divided into three parts. The first part focus on PAH/PSS nanotubes, the second one describes PAH/PSS mats and the last part is dedicated to PAH/PAA nanotubes and mats. Finally, the last chapter summarizes the mains conclusions and introduces some targeted applications of the mats.

Chapter 2

State of the art

2.1 Objectives

This chapter synthesizes all the information collected from the bibliographic searches. As a reminder this master thesis concerns the build-up and the characterization of mats made of nanotubes fabricated by the LbL technique. Nanotubes are thus polyelectrolyte multilayers (PEM). In order to understand and interpret the research results, it is firstly important to fully understand the technique used to produce nanotubes, i.e., the membrane-templated method combined with the LbL technique. As a second step the bibliographical research aims at apprehending the multilayer build-up and the influence of some main processing parameters. And finally the effect of some external conditions on the built multilayer are discussed. The explanation is first detailed for the general case of PEM build-up on a flat substrate, but where possible, the effect of confinement for the particular case of nanotubes is also explained.

2.2 The membrane-templated method

Developped about twenty years ago by Martin et al. the membrane-templated method consists of filling the void spaces of a nanoporous material in order to get tubular nanostructures in high yield. The desired material (metals, polymers, inorganic oxides, semiconductors, etc.) is synthesized or deposited in the pores of the host membrane to replicate the open porosity of the template. There are numerous filling methods such as electroless deposition, electrochemistry, chemical polymerization, chemical vapor deposition, sol-gel deposition, silanization, LbL adsorption, etc. Depending on the filling type the hard templating method produces wires or tubes which can be kept in the pores or released by dissolving the membrane. The structure can also become more complex by combining severals materials to get segmented wires or coaxial tubes for example.[4]

In addition to being simple, versatile and robust, an important advantage of the membrane-templated method with respect to classical techniques is the ability to control precisely the dimensions of the templated membrane: size of the pores, thickness, pore density. And since the length and the outside diameter of the nanotubes are determined by the thickness and the pore size of the membrane respectively, the nanostructures obtained have monodisperse and tunable diameter and length.[5, 6]

In the case of nanotubes another advantage of the templated method is the ability to functionalize the inside and outside surfaces of the nanotube independently of one another and get different surface chemistries. The inside surface is functionalized while the nanotubes are still embedded in the template and when they are released the outer surface becomes exposed and free to be functionalized.[6]

Two types of membrane which are commonly used are track-etched polymer and anodic aluminum oxide membranes. These two templates have well defined cylindrical pores with monodispersed diameter so it allows to obtain monodisperse structures with high aspect ratio. As part of this work, track-etched polymer membranes have been used. The track-etching technique, as depicted in figure 2.1, consists of the irradiation of a nonporous polymeric film of polycarbonate (PC), polyethylene terephthalate (PET) or polyimide (PI) by energetic heavy ions. This irradiation produces some latent linear tracks of locally degraded polymer through the film. This degraded polymer is then removed by a chemical attack to reveal cylindrical pores randomly distributed in the film as imaged in figure 2.2. The diameter of the pores is in the range of 10 nm to 10 μm and depends on the processing conditions such as etching solution concentration and pH, temperature and time. Regarding the porosity, this parameter varies usually between 0 and 20 %.[7]

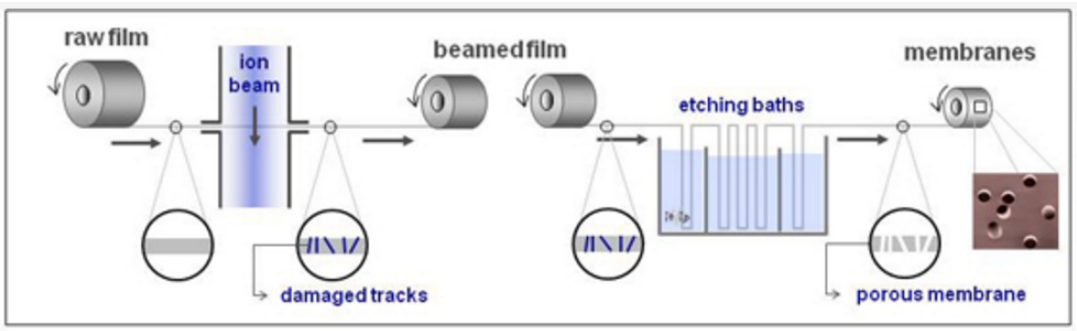

Figure 2.1 – Track-etching technology (the image was excerpted from www.it4ip.be).

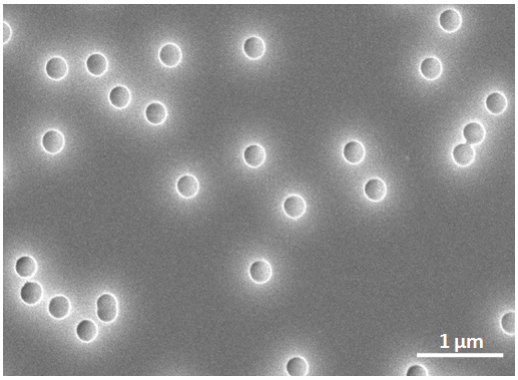

Figure 2.2 – SEM image of the surface of a PC membrane obtained by the track-etched method.

2.3 The layer-by-layer adsorption technique

Among the previously mentioned filling techniques the LbL adsorption stands out for its versatility, simplicity and low-cost. This bottom-up method was introduced in the early nineties by Decher et al. as a coating method.[8] The LbL technique consists of the alternate adsorption of complementary species such as oppositely charged polymers, namely polyelectrolytes, on a charged substrate. The nature of the substrate used is not crucial as long as it has some interactions with the first layer (electrostatic, hydrophobic, etc.). The most common driving force for the alternate adsorption is the electrostatic attraction that controls the build-up process but also the stability of the PEM. Indeed an inversion or suppression of the charge by pH changing, for example, could cause the destruction of the PEM. The applicability of the LbL adsorption can also be widen further by taking benefit from non-electrostatic interactions such as hydrogen bondings, hydrophobic interactions, Van der Waals forces, charge transfer interactions, bio-specific interactions, etc. The range of materials that can be used is quite wide. As long as the alternating charge is maintained LbL assembly can be composed of synthetic polyelectrolytes, biological macromolecules, dye nanoparticles, carbon nanotubes, etc. It is thus compatible with various functional components such as proteins used as polycation or polyanion depending on whether the pH value is under or above their isoelectric point respectively. Furthermore the substrate can also vary according to the form, the size and the nature of the material used (metal, glass, silicon, polymers). In the case of flat macroscopic surfaces or colloids, the LbL technique allows to modify the surface and for porous surfaces it replicates the open porosity, for example to prepare nanotubes.[4, 6, 9, 10, 11]

Electrostatic LbL method uses a step by step process depicted in figure 2.3. First, the solid charged substrate is immersed in the solution of the oppositely charged polyions and adsorbs the first layer. The substrate is then rinsed, with water for example, to remove the non attached material and avoid the contamination of the next solution. The substrate is subsequently immersed in the second polyion solution containing the material of opposite charge which composes the second layer before being rinsed again. These two layers form a bilayer. The process is repeated several times to fabricate the PEM film. An important requirement to produce these films is the charge inversion or charge overcompensation. Indeed, in order to adsorb subsequently oppositely charged polyions the adsorption occurs with non-stoichiometric excess of charge with respect to the previous layer, so that the charge of the substrate changes sign and allows the sequence of the alternate adsorptions.[6] It is also worth mentioning that the nanostructure of the PEM (thickness of the layers) depends on the experimental parameters (pH of the solutions, ionic strength, etc). The effect of these parameters will be discussed in section 2.6.

In the particular case of this work, the complementary species which have been used for the LbL technique are the PAH and PSS polyelectrolytes or PAH and PAA polyelectrolytes. A polyelectrolyte is composed of ionizable monomers that become charged after dissociation in solution and are associated to low molar mass counterions. The conformation of polyelectrolytes in solution is influenced by the interactions between the charged monomers and differs from neutral and uncharged polymer chains. The degree of dissociation of a polyelectrolyte, α, is defined as the fraction of original solute

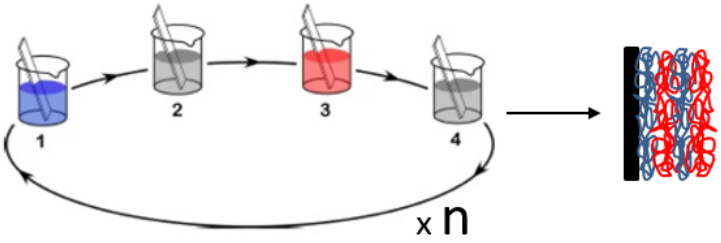

Figure 2.3 – Schematic illustration of the LbL technique which consists of the alternate adsorption of a polycation and a polyanion (1 and 3) with intermediate rinsing steps (2 and 4). The process is repeated n times to produce a PEM with n bilayers. This image was adapted from `http://www.softmattergraduate.uni-freiburg.de/project/2010-2015/B2/b2`.

monomers that is dissociated. According to this value, two categories of polyelectrolytes can be distinguished. If $\alpha = 1$, the polyelectrolyte is *strong* and is slightly influenced by the solution pH such as PSS. By contrast, if $\alpha < 1$ the polyelectrolyte is *weak* and α depends on the solution pH such as PAH and PAA.

2.4 Polyelectrolyte adsorption and multilayer build-up

2.4.1 Ion-exchange model

The simplest adsorption theory that explains the adsorption of polyelectrolytes on an oppositely charged substrate is an ion exchange model.[3] According to this model, polyelectrolytes and counterions are in competition to combine with the charged sites on the surface which is the initial substrate or the previously deposited layer considered as a solid substrate, at least for the first layers. Although the repulsion between charged segments of the chain should prevent the accumulation of charges near the surface, the adsorption is favored by a total gain of entropy, i.e., the system gains more entropy upon counterion liberation than it looses entropy upon polyelectrolyte adsorption. As a consequence, interactions between surface counterions, polyelectrolyte counterions and polyelectrolytes are replaced by surface-polyelectrolyte interactions. This ion exchange induces a quite small enthalpic change so the major free energy contribution is the entropy gain.

Although the ion exchange model can be used to explain qualitatively the influence of some parameters on the PEM build-up such as the effect of the ionic strength, it has some weaknesses. For example, this model can not explain the adsorption of some polycations on net positively charged TiO_2 combining positive and negative charges or the adsorption of amphoteric materials on a opposite net charge surface. The reason for this is that the theory is based on a mean surface potential and does not take into account the heterogeneities of the surface. Therefore other theories, not explained here, which take that into account, have been developped.[3]

2.4.2 Thermodynamics, kinetics and charge overcompensation

It has been experimentally demonstrated that adsorbed polyelectrolyte chains have a small mobility what seems to indicate a nearly irreversible process which can not be explained by the ion-exchange model. Except in some specific conditions with the presence of salt or with low molar mass polyelectrolytes that could enhance the reversibility, polyelectrolyte adsorption is not at thermodynamic equilibrium. For example, it has been shown that a radiolabeled PSS outer layer of a PSS/poly(vinylbenzyltrimethylammonium chloride)(PVBTA) system is not exchanged in the presence of a large excess of unlabeled PSS of the same molar mass. Another experiment has reported that a decrease of pH to 4 for a PSS/poly(dimethylaminoethylmethacrylate)(PAMA) system initially built at pH 8 does not induce a PAMA loss with PSS as outer layer, because, even if the charge of PAMA is increasing since it is a weak polyelectrolyte, the chains are trapped inside the multilayer.[3] PEM should thus be considered as nonequilibrium materials because strong electrostatic forces prevent equilibration processes.[12]

As regards the kinetics of the build-up, the process takes place in two steps. The first kinetic step is a fast mass deposition with a rate of deposition that notably depends on the diffusion of the polyelectrolyte chains. This step takes place within the first minutes, then there is a rearrangement of the adsorbed chains at the surface in a slower step (several hours or days). If the rearrangement of the chains is slower than the deposition step, chains that are anchored by some of their charged sites will not have enough time to rearrange before other chains are attached to neighboring sites. The attachment of new polyelectrolyte chains takes place until the electrostatic repulsion created by the accumulated charges at the surface becomes a barrier. So some sections of the topmost adsorbed chains are anchored while some loops and tails are dangling around and are at the origin of the charge overcompensation.[3]

As it has already been said, this charge overcompensation is necessary for the PEM build-up and will affect the amount of adsorbed polyelectrolytes in the next layer. This means that the adsorbed amount is influenced by loops and tails of the underlying layer which are in turn determined by several parameters. There is for example an influence of the position of the layer in the PEM, loops and tails are different between the first layers influenced by the substrate and the loose outer layer. Indeed for some systems the effect of the substrate causes a nonlinear growth of the layer thickness for the first layers before reaching the linear regime, or an exponential regime for some specific systems, usually before 5 bilayers. Besides the position of the layer for the influence of the substrate, the nature of the substrate should also be taken into account as well as the operational conditions. As it will be discussed in section 2.6 in more details, the ionic strength and pH of the solution can modify the polyelectrolyte charge density or the surface charge density and then also influence the chain conformation and in turn the charge overcompensation. The layer thickness is then not an intrinsic property of the polyelectrolyte.[3]

In the most common systems such as PAH/PSS and poly(diallyldimethylammonium chloride)(PDADMAC)/PSS the observed growth law is linear. But the linear growth is not a generality for all systems. Indeed some combinations of polyelectrolytes can show an exponential growth. This has been observed for example for biopolymers such as

polypeptides and polysaccharides. The origin of the exponential growth is explained by the diffusion of single chains into the PEM during the adsorption steps and since the PEM is thicker after each step the adsorbed amount grows exponentially.[13]

2.4.3 Layer interpenetration

The LbL process would suggest a layer sequence with well separated layered building blocks and sharp internal interfaces. But actually, a layered arrangement with well resolved internal interfaces is not observable neither by x-ray reflectivity nor neutron reflectivity which suggests a large overlap between the segments of adjacent layers.[12] Indeed interdigitation of adjacent species occurs during the PEM build-up. Decher suggested a model of the distribution of polyion segments in PEM film along the surface normal, as shown in figure 2.4.[14] The observed interdigitation is due to both the polymer interdiffusion and the interfacial roughness. To decrease the interdiffusion, some more rigid polyelectrolytes should be used. The distribution width was measured on PSS/PAH systems at $1.5 - 2.5$ bilayers by surface force measurements and electron transfer.[12]

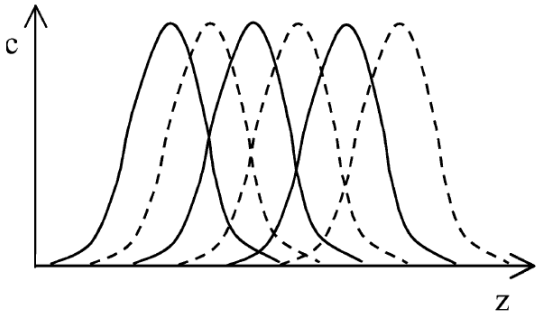

Figure 2.4 – Model of the concentration of polyion segments in PEM film along the surface normal as proposed by Decher. Dashed curves: positive polyelectrolytes; solid curves: negative polyelectrolytes.[12]

2.4.4 Covalent bonding and cross-linking of multilayers

The stability of the LbL multilayers can be insufficient in certain external conditions and becomes challenging for some applications. Indeed electrostatic interactions that are the driving force for the PEM construct could be unstable in solutions with a too high/low pH value or with a high ionic strength, in good solvents of the employed polyelectrolytes, or in solutions with disturbances such as under sonication.[15] If it is necessary the PEM stability can be strengthened by converting weak electrostatic interaction forces into stronger ones such as covalent bonds. These bonds result in a significant improvement of the PEM structural stability.

There are two strategies to get covalently assembled PEMs.[15, 16] The first option is to take benefit from covalent bondings as main driving force for LbL assembly instead of electrostatic interactions. For example, covalently bounded nanotubes were made by using polyethyleneimine (PEI) and poly(styrene-alt-maleic anhydride) (PSMA) as reactive building blocks, bound by amide groups.[16] The second strategy involves a post-crosslinking of the pre-assembled multilayer made of conventional polyelectrolyes.

Several methods to post-crosslink have been developed on the basis of photochemical reactions, thermo reactions or redox reactions.[15]

A common method to increase the stability of PEM structures in the presence of carboxyl groups and primary amines is the post-crosslinking using 1-ethyl-3-(3-dimethyl-aminopropyl)carbodiimide (EDC) and N-hydroxy sulfosuccinimide sodium salt (sulfo-NHS). In the first step, EDC activates carboxyl groups. These activated groups can either spontaneously react with primary amines or they are conjugated with sulfo-NHS to increase reaction efficiency with the amines and stabilize an active intermediate for later reaction with amines, as shown in figure 2.5.[17]

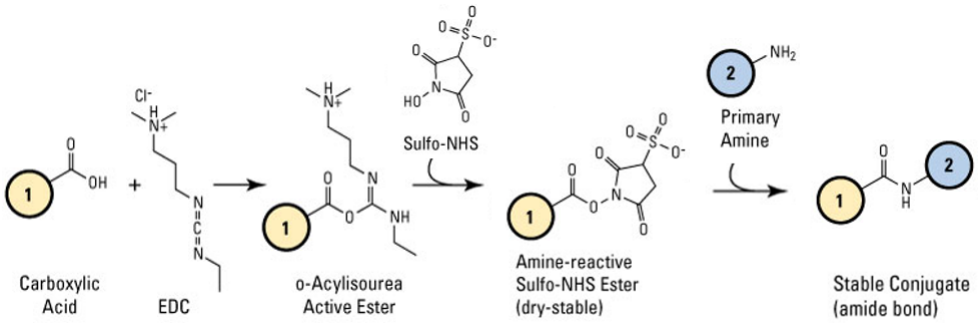

Figure 2.5 – Scheme of the sulfo-NHS plus EDC cross-linking reaction. This image was adapted from [17].

2.5 Growth mechanism of polyelectrolyte nanotubes

The build-up of PEM has been studied by many researchers first on flat substrates.[18] Subsequently researchers became interested in deposition in nanoporous templates but this study is a little bit more difficult since most common characterization techniques are often less appropriate for nanopores. Nevertheless it has been demonstrated that the knowledge regarding flat substrates cannot be transposed to porous substrates. Indeed the confinement of chains in pores affects considerably the growth mechanism of the PEM.

Alem et al. have investigated the effect of the confinement by comparing the LbL deposition of strong polyelectrolytes on flat model surfaces and by alternate filtration within nanopores of track-etched membranes with varying pore diameters. Furthermore the end-to-end distance of the polyelectrolyte chains in solution was tuned by varying the ionic strength of the solutions and the molar mass of the polymers. They obtained a linear growth on flat surfaces for all probed conditions with a growth increment of thickness per cycle of deposition independent of molar mass and substrate nature. By contrast, in the case of nanoporous templates, this growth increment was much larger than on flat surfaces [19], up to 100 times larger in some cases, with the result that the maximum filling of the pore was obtained after one to two cycles. It should be noticed that the filling rate depends also on the type of filling. For example the simple diffusion during immersion of the track-etched membrane leads to a slower filling than a filling by filtration.[4] To explain the rapid filling by filtration Alem et al. suggested that poly-

electrolyte complexation occurs within a dense gel filling the whole nanopore. This gel would be induced by the entanglement of the polymer chains in the confined space of the pore. After the drying of the system the gel collapses and results in nanotubes of thickness directly related to pore diameter.[9] However this mechanism is still not fully understood and is not obvious for the entire scientific community. By contrast with Alem et al. results, Cho et al. showed that the formation of PEM in nanopores leads to thinner walls than on flat substrates due to the restricted polymer entrance into the pores.[20]

In a following study from Roy et al.[4], they observed the growth mechanism in nanoporous templates filled by alternate dipping in polyelectrolyte (PAH and PSS) solutions. In contrast to filtration, the dipping method is more similar to the deposition conditions on flat substrates. The comparison between flat and nanoporous substrates is then more coherent. The parameters investigated in this study are the pore diameter, the molar mass of the polymers and the ionic strength of the solutions which influence the thickness of each adsorbed layer, the interaction between this layer and the pore surface and the rate of diffusion of the chains in the pores. In order to compare growth kinetics for these interconnected parameters, researchers defined a heuristic parameter, Δ_r, that depends on the initial and final pore diameters measured by porometry (see section 3.3) according to the following equation

$$\Delta_r = \frac{d_p(i) - d_p(x)}{d_p(i)} \times 100 \tag{2.1}$$

where $d_p(i)$ and $d_p(x)$ are the initial pore diameter and the pore diameter measured after x bilayer deposition cycles respectively. Defined in this way, Δ_r represents the relative radial PEM increment or the relative gain in PEM thickness as a function of the number of bilayers deposition. The results for three different pore diameters and PAH/PSS systems with low and high molar mass are reported in figure 2.6. This PEM assembly was performed in solution without the addition of salt. Unlike flat substrates for which the growth is linear with respect to the number of bilayers, these results indicate a transition in the growth kinetics for $\Delta_r = 60$ to 70% independently of the ionic strength (not illustrated here) and the polyelectrolyte molar mass. The observation of this transition in the relative radial PEM increment indicates the succession of two regimes with different filling mechanisms. The first deposited bilayers are in the first regime, with $\Delta_r < \sim 70\%$. This regime looks like the growth of a PEM on a flat substrate. But when Δ_r becomes larger than $\sim 70\%$, the growth kinetics slow significantly and the growth enters the second regime (shade region in figure 2.6).

The transition of regimes can be explained on the basis of the reduced variable r_h/r_p where r_h is the hydrodynamic radius of the polyelectrolyte chain and r_p is the pore radius. When r_h is much smaller than r_p such as in the first regime for the first bilayers, polyelectrolyte chains can be considered as rigid spheres for which diffusion in the pore is not a limiting factor. The spheres have a much lower diameter than the pore diameter so the confinement has little effect on the growth mechanism that is similar to the build-up on flat substrates.

Then the wall thickness of the nanotube increases with successive bilayers until the relative gain in PEM thickness is around 70%. It is worth noting that this porometry

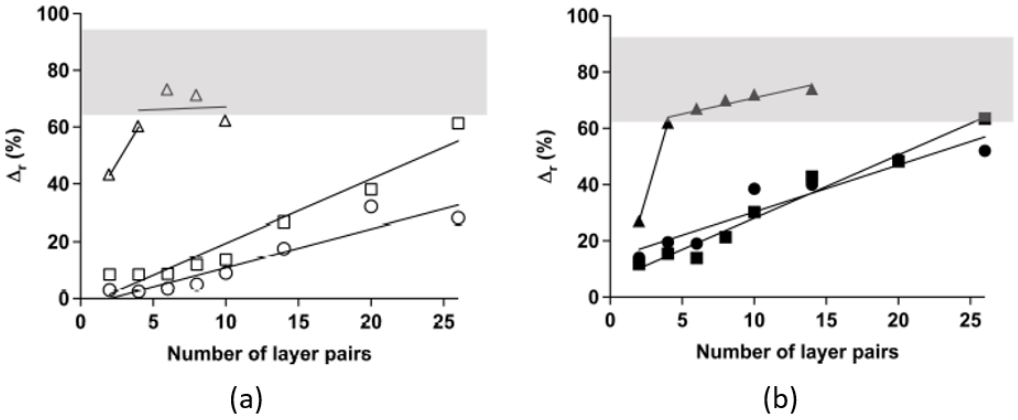

Figure 2.6 – Evolution of the relative radial PEM increment, Δ_r, as a function of the number of bilayers in 100 nm (triangles), 200 nm (circles) and 800 nm (squares) diameter pores. PAH and PSS of low (open symbols) or high (closed symbols) molar mass were used (PSS, low molar mass of $M_w = 17$ kDa and high molar mass of $M_w = 150$ kDa; PAH, low molar mass of $M_w = 15$ kDa and high molar mass of $M_w = 70$ kDa). The absence of values above some number of bilayers indicates that the pores are fully or partially clogged, so that the porometry measurements indicate a zero flow ($\Delta_r = 100\%$). The grey area represents the second regime of which the transition is defined by a change in slope of $\Delta_r(n)$.[4]

value is measured on dry samples and it does not take into account the swelling of the PEM in solution. As discussed in section 2.7.1, the swelling rate for synthetic polymers is between ~ 20 and $\sim 40\%$ in presence of water. Considering this swelling effect, the transition value of 70% in figure 2.6 for the dry state should correspond to pores that become almost filled in the solution. In this regime polyelectrolyte chains begin to form an interconnected network with a lot of entanglements that increase with the number of bilayers to form a denser and denser gel. In this structure r_h and the "effective" r_p are of the same order of magnitude which means that the assumption of rigid sphere for diffusion of polyelectrolyte in the pores is no longer valid. Indeed the confinement has now a significant effect on the growth dynamics which is slowed down because the diffusion becomes a limiting factor. The nanotube growth is then also slowed down. The number of bilayers for which the dense gel is formed depends mainly on the initial pore diameter and probably on the size of the polyelectrolyte chains in solution to a much lesser extent.

The two growth regimes of the nanotube are represented in figure 2.7 before and after drying.

2.6 Influence of the processing conditions on the multilayer build-up

The build-up of PEM is influenced by various parameters and conditions that enable a control of the film properties: ionic strength and pH of the deposition solutions, deposition time, polyion concentration, molar mass of polyions, charge density of the

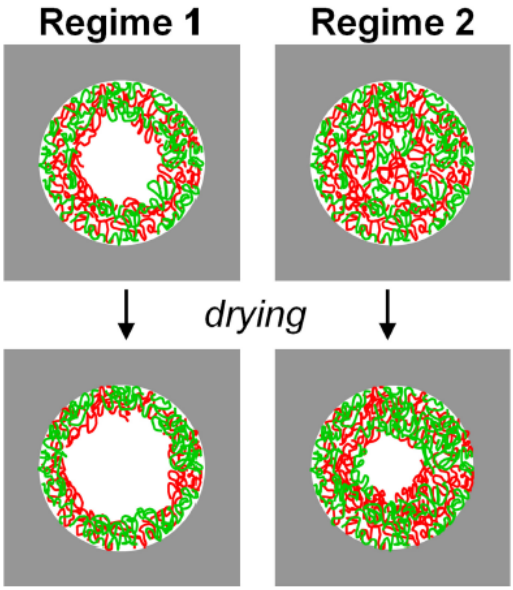

Figure 2.7 – Schematic illustration of the two regimes successively observed during PEM growth in a nanopore, in solution and after drying.[4]

chains, quality of the solvent, salt type, etc.[21] In the literature, the influence of these parameters is again mainly studied for flat substrates. In this section the influence of the main processing parameters are then first explained in the case of a flat substrate before giving some information for each parameter about the effect of the confinement if it has been studied.

2.6.1 Influence of ionic strength and dipping solution pH

A simple model that describes the PEM build-up and allows us to qualitatively understand the influence of some processing parameters on the PEM build-up such as the influence of ionic strength or pH on the PEM thickness is the picture of a "hit and stick" adsorption.[12] The polyelectrolyte chains are adsorbed with their solution conformation onto the surface and then collapse along the surface normal but the lateral relaxation along the surface is neglected. According to the "hit and stick" adsorption, the layer thickness is determined by the area occupied by the chain in solution. If the polyelectrolyte chain has a small radius of gyration and is thus in a small coil conformation, its adsorption will occupy a lower surface area per chain which leads to a larger area density of segments and then a larger layer thickness. Conversely a more rigid chain with a larger coil conformation will cause a smaller density of segments and a smaller layer thickness.

The chain conformation in solution has then a significant role for the thickness. This parameter is controlled by the persistence length which quantifies the stiffness of the chain and is defined as the average distance over which the local orientation of the chain persists. In the case of a charged chain, its persistence length and then its conformation are additionally governed by the electrostatic repulsion of the charges along the chain. If the linear charge increases, the electrostatic repulsion will be stronger and will cause

an increase of the persistence length. Therefore the chain will be in a more extended conformation. One possibility to modify the linear charge is to change the ionic strength of the solution. By increasing the ionic strength, the charge of the polyelectrolyte will be increasingly screened, reducing the persistence length; therefore the coil conformation will be less extended and contain more loops and tails (screening-enhanced regime). However the electrostatic attraction by the surface is also reduced and can induce an adsorption decrease that does not necessarily result in a decrease of thickness (screening-reduced regime) or a desorption.[3] Another point to consider to analyze the influence of the ionic strength is the nature of the salt. Feldötö et al. have demonstrated that the structure of a PAH/PSS PEM was different in presence of KBr or NaCl. Since the bromide ion is larger and has a greater polarizability, the interactions with PAH chains are stronger which causes a larger screening and then a more coiled structure in solution.[21]

For systems using weak polyelectrolytes, the linear charge of the polyelectrolyte can also vary considerably by varying the dipping solution pH since the charged fraction of this kind of polyelectrolyte depends on the local pH of the solution, noting that pH close to the surface is different from that in the bulk of the solution.[3, 12] Furthermore, the pK_a value of a weak polyelectrolyte is different from the solution when it is incorporated in the multilayer since the complexation of the charges can favor the dissociated form of the polyelectrolyte.[13]

It is also important to note that in some cases the solution pH, by modifying the charge density of weak polyelectrolytes, can also affect the growth law. Bieker et al. have studied the multilayer build-up of two weak polyelectrolytes, PAH and PAA, on a flat substrate depending on the solution pH and have identified five distinct pH regimes following different growth mechanisms and growth laws. These differences are explained by the charge mismatch, i.e., difference of the absolute values of the linear charge density of both polyelectrolytes.[13] This analysis, made by dissipative quartz-crystal microbalance (QCM-D) and ellipsometry, distinguishes a central regime (regime III), at intermediate pH values (between 6 and 8), governed by a linear growth. In this regime both weak polyelectrolytes are almost fully charged and can be considered as rigid strong polyelectrolytes. These rigid chains makes strong interactions reducing the interdiffusion and forming a rigid and flat film. A small increase or decrease of the pH value induces a change of regime, the growth law becomes exponential (regimes II and IV). In these regimes the PEM becomes softer and thicker due to a slight charge density mismatch which allows chain interdiffusion: in regime IV, from pH 8 to pH 10, PAA is nearly fully charged and the charge density of PAH decreases; and inversely in regime II, from pH 4.5 to pH 6. In the last two regimes (pH 3 to 4.5 and pH 10 to 12) the growth law is linear again. In these regimes, one polyelectrolyte is almost fully charged and forms flat rigid layers while the other polyelectrolyte has a very small charged fraction and has to form a thicker layer to match the charge per layer. The sketch of the PEM composition depending on the charge mismatch is illustrated in figure 2.8.

In the case of LbL deposition in confined areas such as nanopores, it may be questioned if the influence of the ionic strength is the same. Roy et al. showed that the build-up of PAH/PSS PEM in nanopores leads to a thicker nanotube wall with the number of bilayers in the presence of NaCl. This is consistent with what has been ob-

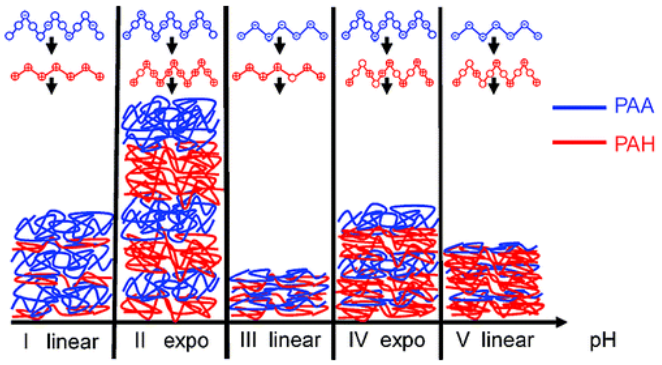

Figure 2.8 – Growth behavior of PAH/PAA PEM depending on charge mismatch.[13]

served on flat substrates: higher ionic strength leads to a more coiled conformation of the chains and then a thicker layer. However, as already indicated in section 2.5, the Δ_r value for the transition of regime seems independent of the ionic strength.[4]

2.6.2 Influence of molar mass

Regarding the molar mass of the polyelectrolytes, the effect on the PEM thickness is not as clear as for ionic strength. For flat substrates it seems that the degree of polymerization does not have a major role in the PEM structure. Lösche et al. have for example studied a PSS/PAH system on flat substrates and demonstrated that an increase from 900 to 5000 for the PSS degree of polymerization induces a change of the overall thickness of $\leq 6\%$.[22] In the case of PEM growth in a nanoporous template, Roy et al. showed that an increase of the PAH and PSS M_w results in a small increase of the PEM thickness. But this effect is related to the pore diameter and was more marked for medium pores (~ 200) than for small or large pores (~ 100 and ~ 500 respectively).[4]

2.7 Response of the multilayer to external conditions

2.7.1 Swelling in humid air and aqueous environment

A PEM is a highly hydrated structure that displays a swelling behavior in air of different relative humidity and in water. Indeed the thickness of the multilayers depends on the degree of humidity. Even at ambient conditions in air usually, but falsely, referred to as the "dry" state, PEMs contain some water and are then slightly swollen. This water content has been calculated on the basis of x-ray reflectivity, neutron reflectivity and FTIR spectra to be on the order of $10 - 20\%$ by weight.[12] This should be taken into account when looking at internal dynamics and stability of the interacting layers because electrostatic forces that govern charge coupling during the build-up depend on the solvent environment, that is the water of hydration.

When PEMs enter into contact with water, as during the build-up, Kugler et al. showed that PAH/PSS PEMs swell by 26% in volume between multilayers dried (0% humidity) and immersed into water.[23] Similar results were found by Elsner et al. who measured an increased in thickness of 30% for the transfer of PAH/PSS multilayers

from air to water.[24] Lösche et al. measured a water concentration slightly larger for their hydrated PAH/PSS film with a $\sim 42\%$ volume fraction. Furthermore they showed that hydration of both polyions was different with ~ 6 H_2O associated with each PSS monomer and only 1 H_2O per PAH monomer.[22] In presence of water, the swelling behavior is also controlled by some physicochemical conditions such as pH and ionic strength (see section 2.7.2).

The water sorption behavior is controlled by the Flory-Huggins interaction parameter, χ, that represents the strength of interaction between two components. For water uptake of the PEMs, χ between the water molecules (mobile phase) and the polyelectrolyte chains have been measured by Kügler et al.: $\chi = 0.91 \pm 0.05$ for PAH/PSS PEM which means that the water molecules interact more strongly with themselves than with the polyelectrolytes. Therefore, even if PAH and PSS are hydrophilic polymers, the PEM is rather hydrophobic. This observation is explained by the charge screening in the bulk that suppresses the ionic character of the polyelectrolyte. By contrast this is not the case for the top layer for which contact angle measurements indicate that it is hydrophilic. Indeed screening of positive or negative charges is missing on the top layer.[23]

Hydration of PEM causes its swelling and then an increase of its thickness but the reverse process is also possible since dehydration leads to shrinkage of the multilayers. However on average $\sim 40\%$ of the liberated water volume due to the removal of water molecules become a void volume upon shrinkage. Indeed the polymer chains do not fill this whole volume, probably due to steric hindrance in the polymer chains.[22]

It is worth emphasizing again that values given in this section have been measured for flat films and do not take into account a possible effect of the confinement in nanopores.

2.7.2 Influence of pH

We have seen previously that the pH of the dipping solution influences the structure of the PEM in formation but we can also take advantage of this influence after the PEM formation. This has been for example shown by Chia et al. who demonstrated the existence of a pH-responsive reversibly swellable PAH/PAA nanotube arrays.[25] They showed, as represented in figure 2.9, that a transition from a high pH solution (≥ 5.5, state B) to a low pH solution (≤ 2.0, state A) induces the protonation of the carboxylate groups of PAA polyelectrolyte chains and then a significant swelling due to the breakage of NH_3^+-COO^- ionic links between the two polyelectrolytes. Inversely, the transition from low pH to high pH induces a decrease of the swelling since ionic links are regenerated. Following path 4 and drying the PEM from low pH, it will collapse to form a dense structure (state C) because the mobility of the chains is high enough to allow water rejection which is not the case for path 2. Indeed upon drying at high pH value, micrometer sized pockets of water are trapped and lead to air pockets in the dry structure. pH-induced swelling-deswelling transition in the wet state is thus related to a porosity transition in the dry state.

Lee et al. have also taken advantage from the effect of the pH on the PEM construct by developing a pH-responsive nanoporous membrane that shows discontinuous

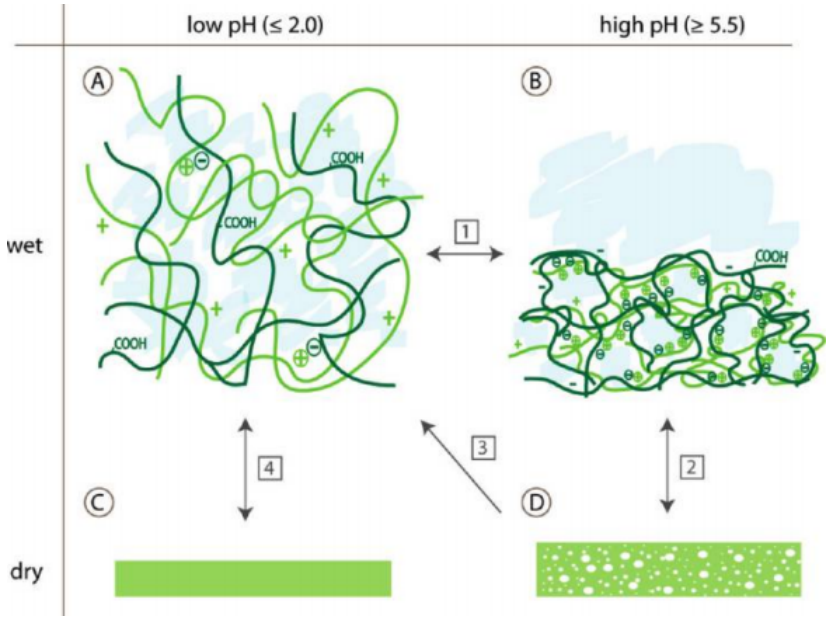

Figure 2.9 – Sketch of a PAH/PAA multilayer film depending on the pH (high or low) and humidity conditions (wet or dry).[25]

changes in its permeation properties. The PAH/PSS multilayers in the track-etched PC membrane have a pH-induced swelling/deswelling behavior which can serve as a hysteretic gating, i.e., both "closed" and "open" states can be achieved at one pH condition depending on the pretreatment history. Therefore this property is interesting for some applications such as drug delivery, chemical sensors, separation of macromolecules, etc. Furthermore this study has shown a smaller swelling of the multilayer in nanopores compared to the same multilayers on flat substrates and under the same conditions which is explained by a decrease in the volume available for the swelling PEM in confined geometries.[19]

2.8 Nanotube applications and filamentous membranes

The combination of LbL assembly with the nanoporous template method is at the origin of numerous and varied, complex and functional nanotubular structures thanks to both the diversity of LbL building elements and the tight dimensional control of the template method. This variety offers many possibilities in various fields of application. Among these applications, nanotubes could for example be exploited as soft nanoactuators by taking advantage of the swelling behavior of two weak polyelectrolytes in the presence of pH variations as described in section 2.7.2. In this example the pH variation induces nanoscale conformational changes allowing a macroscopic structural variation. The use of proteins as LbL building elements to form protein nanostructures has also a great potential for many biomedical applications such as biosensors, enzymatic bioreactors, bioseparations or drug delivery.[26] Instead of directly incorporating proteins as building elements, the nanostructure can also be functionalized with proteins after the LbL deposition. Furthermore some applications also use template membranes with embedded nanotubes left within the pores. These free-standing nanotube-containing membranes

can have several applications as separation membranes for ionic species, nanomembranes with adaptable transport properties or catalytic membranes since LbL technique is compatible with the incorporation of metal colloids or nanoparticles in the PEM structure without inhibiting access to catalytic sites.[16, 27]

For biological applications or drug delivery that require to release nanotubes from the template, the nanotube dispersion in aqueous media turned out to be very difficult since nanotubes tend to adhere irreversibly on surface filters and between themselves. Researchers have then developped different techniques to improve the dispersing without damaging nanotubes. In this context, Saghazadeh et al. have developed an universal method to transfer membrane-templated nano-objects to aqueous solutions.[5, 28] The first idea was to improve the dipersion but they found that nanotubes can also form a mat and thus create a membrane which combines the advantages of the nanotubes and those of filamentous structure: high surface-area to volume ratio, large flexibility with regard to the materials used and modification of the surface chemistry. Until now no article has studied the interest of such mats of LbL nanotubes. Currently the most common method to produce filamentous membranes is electrospinning technique. These membranes are used as air or water filters, membrane bioreactor or biosensor by using enzyme-immobilized membranes, etc.[29, 30] In this work, we will thus investigate in details the morphology and properties of mats of LbL nanotubes.

Chapter 3

Experimental section

3.1 Materials

Poly(sodium 4-styrenesulfonate) (PSS, M_w : 70 kDa) and 1-ethyl-3-(3-dimethylaminopropyl)carbodiimide (EDC) were purchased from Acros organics. Poly(acrylic acid) (PAA, M_w : 100 kDa, 35 wt. % in H_2O) and poly(allylamine hydrochloride fluorescein isothiocyanate) (PAH:FITC, M_w : 15 kDa) with a monomer to dye ratio (PAH:FITC) of (50:1) were purchased from Sigma Aldrich. Poly(allylamine hydrochloride) (PAH, M_w = 120 to 200 kDa) was purchased from Alfa aesar. Poly(allylamine hydrochloride rhodamine B isothiocyanate) (PAH: RITC, M_w : 150 kDa) with a monomer to dye ratio (PAH: RITC) of (296:1) was purchased from Surflay in solution (10.47 mg/ml). N-hydroxy sulfosuccinimide sodium salt (sulfo-NHS) was purchased from ProteoChem. The structures of PSS, PAH and PAA are presented in figure 3.1.

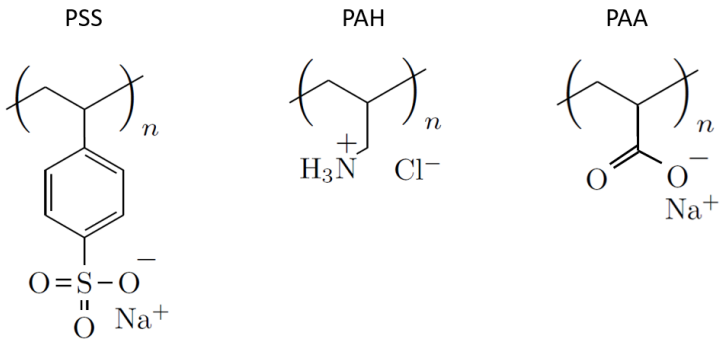

Figure 3.1 – Chemical structure of PSS, PAH and PAA polyelectrolytes.

Sheets of track-etched PC membranes were provided by It4ip (Louvain-la-Neuve, Belgium, `http://www.it4ip.be`) with nominal pore diameters of 100, 300 and 800 nm. The first two membranes had a thickness of 25 μm and the third one had a thickness of 24 μm. These membranes had a pore density of $\sim 6 \times 10^8$, 1×10^8 and 4×10^7 pores·cm^{-2} respectively. Hydrophilic poly(ethylene terephthalate) (PET) membranes with a pore size of 200 nm, thickness of 23 μm and pore density of $\sim 5 \times 10^8$ pores·cm^{-2} were provided by It4ip as well. The PET membranes were cut in circles with a cookie cutter of two different diameters. Small and large circle diameters measure 12.5 and 26 mm respectively.

3.2 Assembly of polyelectrolyte multilayers

Polyelectrolyte solutions were freshly prepared before each use, except for PAH-FITC and PAH-RITC solutions which were reused, at a concentration of 1 mg/ml. Milli-Q water with 18.2 MΩ·cm resistivity was used in all experiments. Each solution was stirred during 30 minutes before use and controlled for its pH thanks to a pH-meter. The pH of PAH and PSS solutions has an average value of 4.0 and 5.3 respectively and was not modified. The initial pH of the PAH-FITC solution was 6.6 on average. To get a pH value around 4.0 as for the PAH solution pH and work in the same pH conditions, the PAH-FITC solution was modified with the addition of HCl (1 M). The pH of the PAH-RITC solution was measured around 3.9 and not modified since the value was close to the PAH solution pH. In the particular case of the PAH/PAA system, the pH of all the solutions were adapted at 5.5, including the rinsing water.

The build-up of PAH/PSS multilayers with n bilayers in nanopores was performed by alternatively dipping the PC template in PAH and PSS solutions for 30 minutes each (figure 3.2). Between each adsorption step, the PC template was rinsed in two different baths of milliQ water (3 min each) to remove unadsorbed materials. This process was repeated n times to obtain n bilayers. The process was identical for the build-up of PAH/PAA, PAH-FITC/PSS and PAH-RITC/PSS multilayers, except that for both labeled PAH, the nanotube build-up was performed away from light. To limit the formation of a film on the top and the bottom surfaces of the membrane leading to the encrusting of the pores, the membrane was decrusted after each bilayer, every third bilayer or only at the end of the build-up depending on the desired decrusting. This step consists of scrubbing the top and bottom surfaces of the PC membrane with a cotton swab to eliminate these adherent layers.

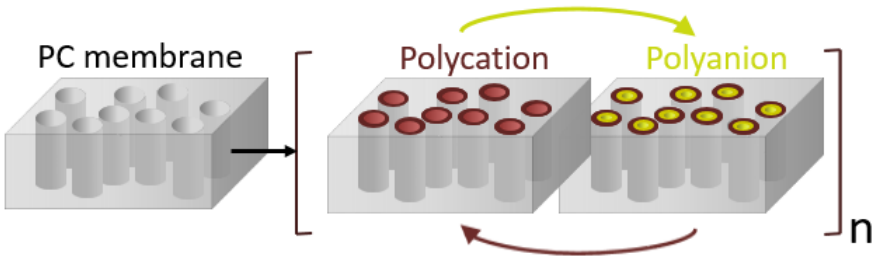

Figure 3.2 – Scheme of the assembly of polyelectrolyte multilayers in the nanopores of a track-etched PC membrane through the alternate adsorption of a polycation and a polyanion. The number of cycles corresponds to the number of bilayers.

The cross-linking of PAH/PAA multilayers was performed when nanotubes are still entrapped in the template. The PC membrane containing the nanotubes was immersed, for one night, in a solution with 100 mg/ml of EDC and 11 mg/ml of sulfo-NHS freshly prepared immediately prior to use. The solvent was milliQ water with NaCl 0.15 M and the solution pH was adjusted at pH 5.

3.3 Characterization of polyelectrolyte nanotubes

Gas-flow porometer

In order to study the *growth of the PEM* in the track-etched PC membrane nanopores, gas-flow porometry measurements were performed on PC template containing the nanotubes. A porometer provides an average diameter of the nanopores which can vary depending on experimental conditions (number of bilayers, decrusting frequency, etc.). All samples were air-dried, fixed on a holder, with an effective area of 0.137 or 0.394 cm^2 depending on the initial pore diameter and analyzed at ambient temperature. The measure achieved by the flowmeter (GMF Pro Gas Flowmeter) consists of delivering nitrogen gas upstream the sample and measuring the air flow (ml/min) downstream. The upstream pressures used were 2, 0.47 or 1 bar for PC membranes with a pore diameter of 100, 300 and 800 nm respectively. The average nanopore diameter is calculated from the resulting air flows by using relationships based on the Knudsen diffusion and the viscous flow (Hagen-Poiseuille). The flux (mol/m^2 s) related to these two mechanisms are defined according to the following equations respectively

$$J_{diff} = \frac{4}{3}\frac{d}{l}\frac{(P_{up} - P_{down})}{\sqrt{2\pi MRT}} \tag{3.1}$$

and

$$J_{visc} = \frac{d^2}{l}\frac{(P_{up}^2 - P_{down}^2)}{64\mu RT} \tag{3.2}$$

where d is the pore diameter (m), l is the thickness of the PC membrane (m), P_{up} and P_{down} are the pressures (Pa) upstream and downstream from the sample respectively, M is the gas molar mass (kg/mol), μ is the dynamic viscosity of the gas (kg/m s), R is the ideal gas constant (J/K mol) and T the gas temperature (K). The total volume flow rate Φ (m^3/s) resulting from both Knudsen diffusion flux and viscous flux is calculated from

$$\Phi = (SP)\frac{RT}{P_{atm}}(J_{diff} + J_{visc}) \tag{3.3}$$

where S is the effective section area of the membrane (m^2), P_{atm} is the atmospheric pressure (Pa) and P is the transparency of the membrane expressed as

$$P = N\frac{\pi d^2}{4} \tag{3.4}$$

where N is the pore density (m^{-2}).[4] For each sample the measured value of the total volume flow rate is an average of at least 10 measurements.

Scanning electron microscopy and atomic force microscopy

The *morphology of the PC template* containing the LbL nanotubes was imaged by scanning electron microscopy (SEM) and atomic force microscopy (AFM). For SEM analysis, the samples were metallized with a 8 nm layer of chromium and then imaged using a JEOL 7600F SEM operated at 5 or 10 kV. For AFM, the analysis was performed in air with ScanAsyst-air probes in peak force tapping mode (PeakForce QNM) with a Bruker

Multimode Nanoscope VIII. Acquired AFM results were processed using a macro implemented by A.M. Jonas, H. Haubruge and B. Nysten on Igor Pro 6.37 software (Microscopy Image Processing and Analysis v15.02.19). A second-order flattening procedure (whole image mode) was performed on all AFM images.

For the characterization of the nanotubes themselves, a step of releasing from the template was performed. After air-drying, the PC membrane was dissolved in CH_2Cl_2 with subsequent sonication during 10 times one second resulting in a colloidal suspension of nanotubes and dissolved PC in CH_2Cl_2. The nanotubes were then recovered by the filtration of this solution over a small circle of nanoporous PET membrane. At the end of the filtration, fresh CH_2Cl_2 was filtered to limit the presence of remnant PC. The PET membrane was then air dried to allow the rapid solvent evaporation and then preserved in an aluminium wrapping.

The *morphology of the obtained LbL nanotubes* was determined by SEM. For this analysis, the CH_2Cl_2 solution containing the nanotubes was filtered through a PET filter coated with a 20 nm layer of gold. Samples were observed with a JEOL 7600F SEM operated at 15 kV. To get the persistence length of the extracted nanotubes and then an evaluation of the rigidity, SEM images were analyzed thanks to a macro implemented by A.M. Jonas on Igor Pro 6.37 software. By drawing and following the contour of the nanotubes (see an example in figure 3.3), the macro measures for each tube the contour length and its end-to-end distance. The average contour length, L, of the nanotubes and their root-mean-square end-to-end distance, R_{EE}, are calculated from these values. Under the assumption of an infinitely long rope, the ratio $\frac{R_{EE}^2}{L}$ is equal to $2L_p$ with L_p the persistence length of the rope. However if the rope length is much smaller than its persistence length, the ratio equals L. Therefore, the ratio $r = \frac{R_{EE}^2}{L^2}$ varies between $\frac{2L_p}{L}$ and 1 and is an index quantifying the flexibility of the nanotubes relatively to their length. A smaller value indicates a more flexible nanotube. The measurements of R_{EE} and L have been performed on 30 nanotubes for each system to obtain an average value.

These measurements are also related to the Young's modulus of the material, E. Assuming that the chain is infinitely long, the persistence length of the chain is defined by equation 3.5. This value is related to the Young's modulus according to equation 3.6 where B_s is the bending stiffness, k_B is the Boltzmann constant, T is the temperature and I is the second moment of inertia.[31] For a tubular shape, I depends on the inner and outer radius of the tube, r_i and r_o, according to equation 3.7. Therefore measurements of the nanotube geometry (R_{EE}, L, r_i and r_o) enable to calculate the Young's modulus of the material.

$$L_p = \frac{R_{EE}^2}{2L} \tag{3.5}$$

$$L_p = \frac{B_s}{k_B T} = \frac{EI}{k_B T} \tag{3.6}$$

$$I = \frac{\pi}{4}(r_o^4 - r_i^4) \tag{3.7}$$

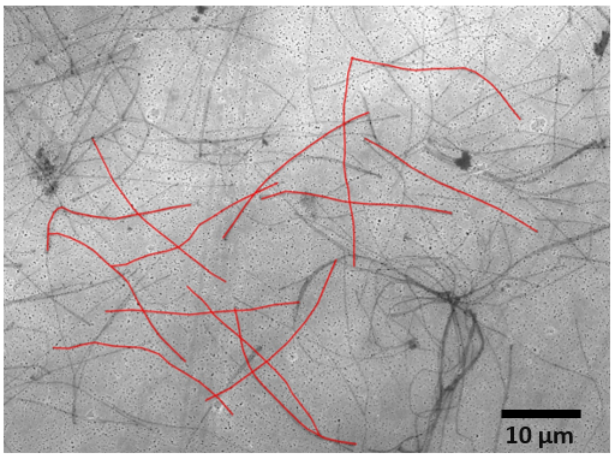

Figure 3.3 – Processing of a SEM image of PAH/PSS nanotubes by a macro implemented by A.M. Jonas on Igor Pro 6.37 software. The macro measures the contour length and the end-to-end distance of each distinguishable nanotube by drawing and following the contour of the nanotubes.

3.4 Build-up of mats

In order to build a mat of nanotubes, the first step is to extract the nanotubes from the PC membrane by dissolving the membrane in CH_2Cl_2. Subsequently these solutions are sonicated for 10 times one second and then alternatively filtered with fresh CH_2Cl_2 through a nanoporous PET membrane metallized with a layer of 20 nm of gold. At the end of the filtration, fresh CH_2Cl_2 is filtered again to limit the presence of remnant PC. The filtration system is connected to a pump according to figure 3.4. The nanotubes are thus accumulated on the PET membrane to form a mat of entwined nanotubes. The mat is air dried to allow rapid solvent evaporation and then preserved in an aluminium wrapping.

3.5 Characterization of mats

Microscopies to observe the morphology

Several microscopy observations were performed to characterize the *morphology of the mats*: SEM, AFM, fluorescence microscopy, confocal laser scanning microscopy (CLSM) and optical microscopy. For the SEM and AFM analyses, the samples were imaged without any further preparation. The SEM used was a JEOL 7600F operated at 5 kV. For AFM, the analysis was performed in peak force tapping mode (PeakForce QNM) with a Bruker Multimode Nanoscope VIII. It was carried out in air with ScanAsyst-air probes and in water with ScanAsyst-fluid probes in a fluid cell (Bruker). Acquired AFM results were processed using the same macro as for the characterization of the PC template on Igor Pro 6.37 software. A second-order flattening procedure (whole image mode) was also performed on the images.

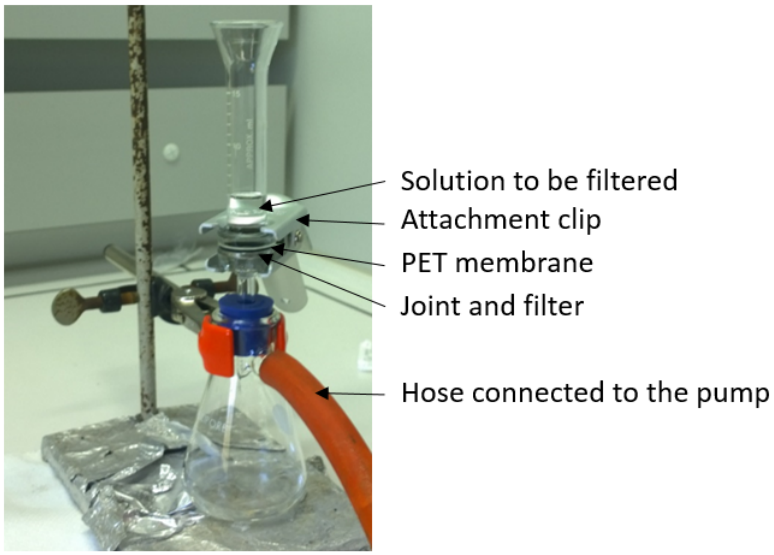

Figure 3.4 – Filtration system used to build mats of nanotubes.

Mats made of fluorescently-tagged nanotubes were characterized by fluorescence microscopy to get some additional information on the *morphology* and on the *lateral homogeneity* of the mat. For this experiment, the mat was placed between two glass slides. Samples were imaged with an Olympus IX71 inverse epifluorescence microscope with x10, x20 and x40 objectives and equipped with red and green filters. In cases for which the mats were tagged with both FITC and rhodamine fluorescent markers, images from the same area were further processed with the "Cellsens Dimension 5D" software associated with the microscope in order to combine data.

The *morphology* of the mats as well as their *vertical homogeneity* were analyzed by CLSM on mats made of fluorescently-tagged nanotubes. The mats were again placed between two glass slides. Samples were imaged with a Zeiss LSM 710 microscope with x25 and x63 objectives and equipped with green and red filters. For samples imaged with the x63 objective, some oil was used between the objective and the sample to improve the quality of the acquired data. Imaging was performed in the stack mode which allows a three-dimensional reconstruction from parallel plans with a space between them of 0.37, 0.4 or 1 μm. Data were further processed with ZEN 2.1 (black) software from Carl Zeiss Microscopy. Subsequently data of the cross-sections were analyzed on Matlab R216a software. For each cross-section, the corresponding 3D image was treated in Matlab to align peaks along the length and then take an average profile as seen in figure 3.5. The measurement of full width at half maximum allows to relatively compare the thickness of each mat. It is important to note that the error on the full width at half maximum is proportional to the spacing between the planes of the stack.

Finally the samples were also imaged by optical microscopy after a cutting step by cryomicrotomy. The cryomicrotomy was performed with a LEICA FM FC6 device in presence of nitrogen at $-40°C$. The sample was in contact with a water drop, solidified by the nitrogen gas, to add rigidity to the sample and to avoid deformations during the

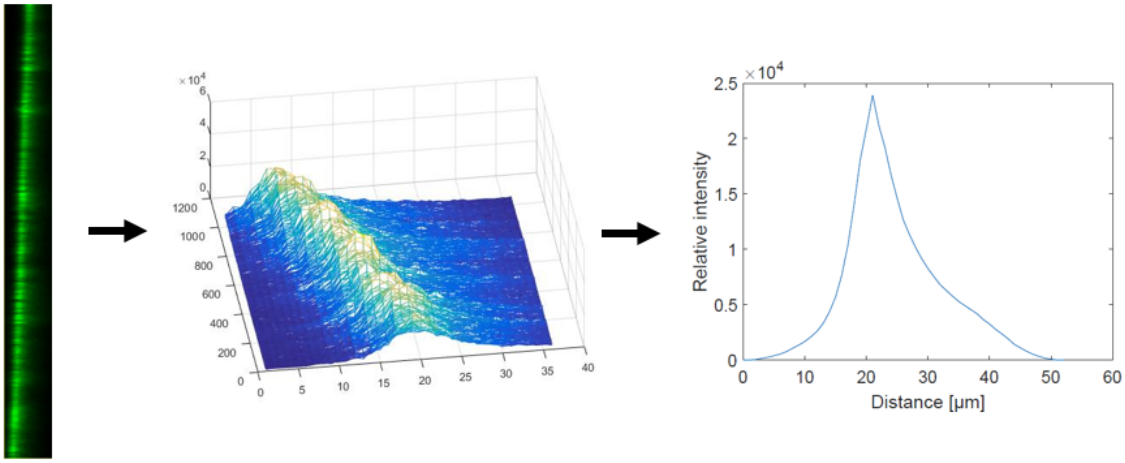

Figure 3.5 – Steps of the Matlab analysis of mat cross-sections obtained by CLSM to measure full width at half maximum of the average profile.

cut. After the cut the section was recovered on a solution of 60% of dimethyl sulfoxide (DMSO) and 40% of water. The optical microscope was an Olympus AX70/Provis used in transmission in the phase-contrast mode with a x100 objective.

Time of flight - secondary ion mass spectrometry

The *chemical composition* of the mats has been examined by time of flight - secondary ion mass spectrometry (ToF-SIMS) to check the presence of undissolved PC on the mat. ToF-SIMS spectra were obtained using a IONTOF 5 (Muester, Allemagne) with an ion beam of $Bi5^+$ (30 keV). The analysis area was 300 μm x 300 μm and the primary ion dose density was 4.49 x 10^7 ions/cm^2. Two spectra were acquired in conventional static mode for each sample.

Atomic force microscopy in force spectroscopy mode

Besides the morphology observation, AFM was also used to determine the *Young's modulus* of the mat by force microscopy. For this purpose, the analysis was performed on a Bruker Icon Dimension with sensors with integrated colloidal particles. Two different sensors were used in order to carry out the experiment with two different cantilever stiffness constants. The colloidal particle for the first sensor was made of SiO_2, had a 6.62 μm $\pm$10% diameter and its stiffness constant was 2.94 N/m. This last value has been calculated for the thermal tuning calibration. For the second sensor, the material of the colloidal particle was borosilicate glass. The particle had a 5 μm $\pm$10% diameter and a stiffness constant of 53.6 N/m. Since the resonance frequency of the sensor was announced above 200 kHz, the thermal tuning calibration was not appropriate to measure the force constant. Therefore a java application developed at the university of Melbourne was used instead.[32] The required data for this calculation were the exact dimensions of the cantilever. To get these information, this second sensor has been fixed

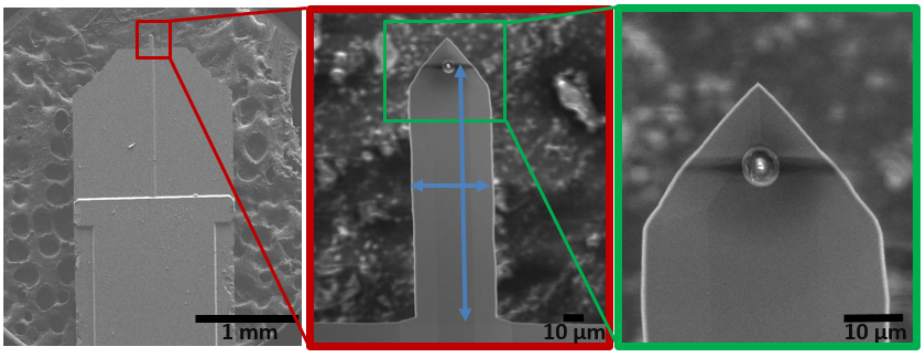

Figure 3.6 – SEM images of an AFM sensor with a colloidal particle at the end of the cantilever. Blue double arrows indicates the necessary dimensions to calculate the stiffness constant of the cantilever.

on an holder and imaged by SEM as seen in figure 3.6. The width and length of the cantilever, as indicated by blue double arrows in figure 3.6, measured 41 and 121 μm respectively.

Samples were scanned in "Force-Volume" and "Point and Shoot" modes for softer and stiffer sensors respectively. These two modes are used to collect force curves over an image area as represented in figure 3.7. For the first mode the positions of the scanned points are in an array that can not be precisely placed on the image but the number of curves can be very large. By contrast, for the "Point and Shoot" mode, the points can be manually placed on the topographical image of the sample but the number of curves is limited because of a longer data processing. The mode choice for both sensors has been made during the experiment in order to limit the number of improperly-measured curves. Acquired data were analyzed by the Nanoscope Analysis v.1.5 software (Bruker). To determine the surface elastic modulus, tip-surface interaction forces from the retraction curve are modeled by the DMT model which takes into account both adhesive and repulsive forces. According to [33], this model is based on three assumptions:

- there is no deformation outside the contact area;
- deformation inside the contact area obeys the Hertz theory;
- adhesion is due to long-range attractive (Van der Waals) forces outside the contact area.

The contact stiffness, k_N, between the tip and the surface is defined as the first derivative of the load, F, with respect to the penetration depth and is equal to $2aE^*$ where a is the contact area radius (figure 3.8) and E^* is the reduced modulus (see equation 3.8).[33]

$$k_N = \frac{\partial F}{\partial \delta} = 2aE^* \tag{3.8}$$

E^* and a are defined by equations 3.9 and 3.10 respectively where ν_1 and ν_2 are the Poisson ratios of the tip and the sample, E_1 and E_2 are the Young's modulus of the tip

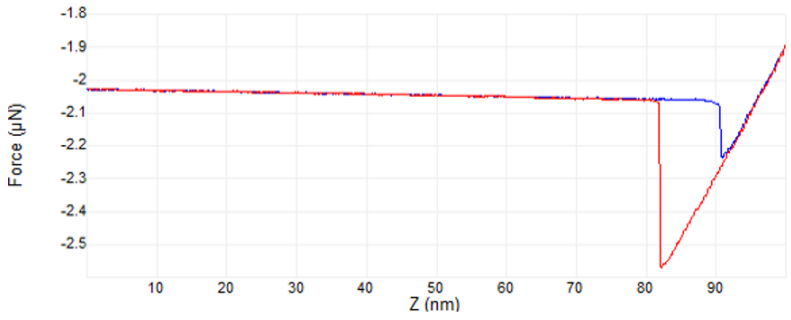

Figure 3.7 – Example of AFM measurement of cantilever force (F) depending on the tip-surface separation (Z). The blue curve is the approach curve and the red one is the retraction curve.

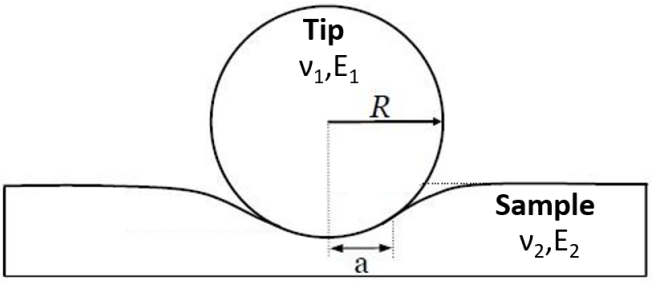

Figure 3.8 – Parameters of the tip, the sample and the contact area.

and the sample and R is the contact radius of curvature. The latter is equal to the tip radius of curvature since the sample surface radius may be considered as infinite.

$$\frac{1}{E^*} = \frac{1-\nu_1^2}{E_1} + \frac{1-\nu_2^2}{E_2} \tag{3.9}$$

$$a^3 = \frac{3}{4}\frac{RF}{E^*} \tag{3.10}$$

Since the modulus of the tip is much larger than the sample's modulus, the reduced modulus is simplified and takes only into account the sample's parameters according to equation 3.11. The contact stiffness can thus be calculated from equation 3.12.

$$E^* = \frac{E}{1-\nu^2} \tag{3.11}$$

$$k_N = 2\sqrt[3]{\frac{3}{4}\frac{RF}{E^*}}E^* \tag{3.12}$$

Chapter 4

Results and discussion

This chapter is divided in three sections. The first section presents the results and discussion related to the assembly and the characterization of nanotubes for the model polyelectrolyte combination consisting of reference synthetic polyelectrolytes PAH and PSS. The next section focuses on the characterization of mats built from the nanotubes characterized in the first section. And the last section is dedicated to nanotubes and mats made of the two weak polyelectrolytes PAH and PAA.

4.1 Characterization of the nanotubes

This section will look at the effect of some processing parameters of the nanotube assembly such as the number of bilayers and the decrusting frequency on growth and morphology of the nanotubes. The objective of this first investigation is to select the optimal conditions to assemble nanotubes that will be used to form mats.

4.1.1 Growth of PAH/PSS multilayers in nanopores

A first aspect that was important to understand was the growth of PAH/PSS multilayers in PC nanopores depending on the number of bilayers and the decrusting frequency. The PEM growth was first observed in nanopores with a diameter of 300 nm. In order to do that, samples have been prepared with a varying number of bilayers from 1 to 9. Furthermore two frequencies of decrusting have been analyzed in parallel: decrusting after each bilayer and decrusting only once at the end of the assembly, resulting in 18 samples which have been analyzed by porometry. The results, presented in figure 4.1 **a**, show that the pore diameter decreases with an increasing number of bilayers for both frequencies of decrusting. This indicates a corresponding increase in the average multilayer thickness on the template walls.

In the case of decrusting after each bilayer (squares on the graph), two regimes can be observed. The first regime from 1 to 6 bilayers is almost linear. Then the 6^{th} bilayer marks the transition to the second regime, the growth slows abruptly and the pore diameter seems to keep constant with increasing bilayers. In order to compare the growth evolution for different pore sizes, as it will be done later on, the pore diameter data are used to calculate the relative radial PEM increment (Δ_r) (as defined in equation 2.1, see

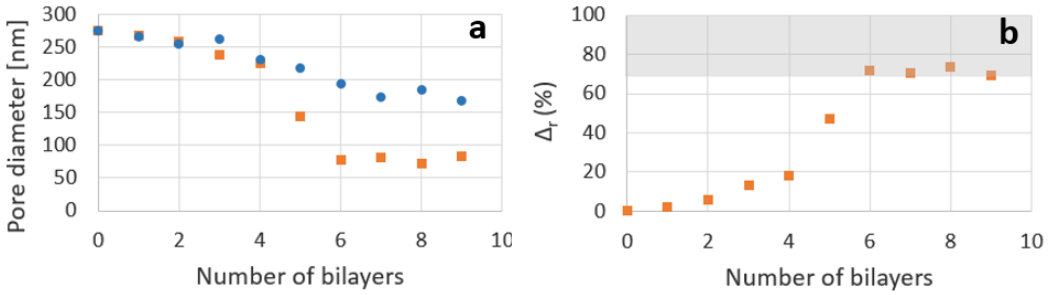

Figure 4.1 – (a) Evolution of the pore diameters estimated by gas-flow porometry and (b) evolution of the relative radial PEM increment as a function of the number of bilayers for samples with an initial diameter of 300 nm and decrusted after each bilayer (orange squares) or decrusted at the end of the assembly (blue circles).

section 2.5) in figure 4.1 **b**. These results indicate a transition in the growth kinetics at 6 bilayers for $\Delta_r \simeq 70\%$ as it has been observed by Roy et al for PAH/PSS multilayers in nanoporous templates.[4] Below 70%, the filling mechanism is similar to the growth of a PEM on a flat substrate and is linear. But above this transition value, the confinement effect becomes significant. An interconnected network of polyelectrolyte chains is formed and the diffusion becomes limiting so that the growth dynamics is slowed down.

By comparing results for the two frequencies of decrusting, it is shown that, after 4 bilayers, samples decrusted only once at the end of the build-up have on average a larger pore diameter and thus a thinner PEM thickness. The final thickness after the adsorption of 9 bilayers is around 100 nm with a decrusting after each bilayer compared with about 55 nm with only final decrusting. The reason for this difference is that, during the PEM formation, a PEM film is also formed on the top and bottom surfaces of the template and these films encrust the pores and limit the diffusion of the polyelectrolyte chains through the pores. If these films are removed after each bilayer, the following layer will not be affected by the crusting, but if they are not the PEM growth slows with the increasing crusting and the PEM thickness is thinner than the corresponding sample decrusted after each bilayer.

In order to limit the number of decrusting steps which are relatively tedious, it has been proposed to decrust the PC membrane only every third bilayer, so after 3, 6 and 9 bilayers. Indeed it can be seen in figure 4.1 **a** that the decrusting for the first layers is not necessary since there is no difference before 4 bilayers and it can be assumed that a less frequent decrusting for the following bilayers can be a suitable compromise. This assumption is verified in figure 4.2. Samples decrusted every third bilayer (triangles on the figure) have the same (for 3 bilayers) or a similar (for 6 and 9 bilayers) pore diameter as the corresponding samples decrusted after each bilayer.

In order to understand the influence of the pore diameter of the template membrane on the PEM growth, porometry tests were also performed on PC membranes with pore diameters of 100 and 800 nm. Data were also recorded for PEMs with 1 to 9 bilayers and the decrusting was done after each bilayer or every third bilayers. Results for the 100 nm pore diameter are illustrated in figure 4.3. For some samples the calculated gas flow was not constant during measurement which means that the samples were damaged

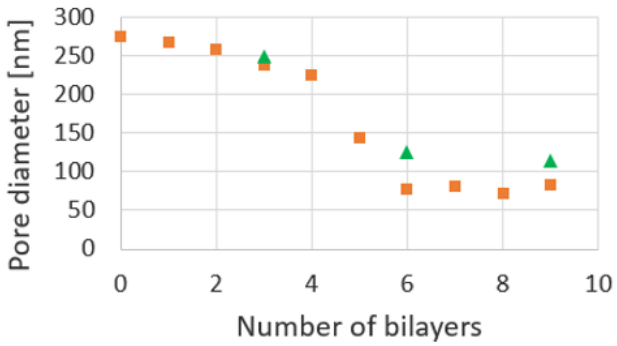

Figure 4.2 – Evolution of the pore diameters estimated by gas-flow porometry as a function of the number of bilayers for samples with an initial diameter of 300 nm and decrusted after each bilayer (orange squares) or decrusted every third bilayer (green triangles).

and cracked with the applied pressure, probably due to a too strong decrusting (open symbols). Therefore these data should not be taken into account. In figure 4.3 **b**, two growth regimes are observed with the second one that is slower in terms of kinetics. Such as for membranes with 300 nm pore diameter, the change in the evolution of the radial PEM increment appears when it reaches a value around 70%. This value corresponds to almost completely filled pores due to the swollen state of multilayers when they are in presence of water. However this transition occurred more rapidly for these smaller pores: at 5 bilayers instead of 6 for 300 nm pores. Data with a lower decrusting frequency do not provide a lot of information since two of the three values should be rejected but it can still be concluded that the PEM thickness of a sample with 6 bilayers which has been decrusted after 3 and 6 bilayers is similar to the corresponding sample which has been decrusted after each bilayer. The decrease of the decrusting frequency is thus acceptable in this case.

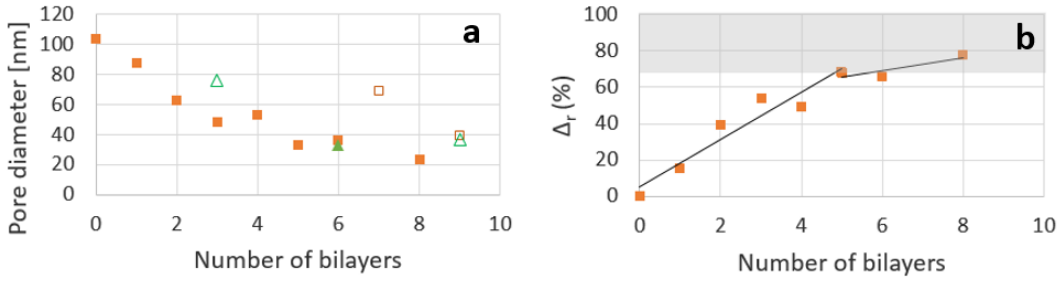

Figure 4.3 – (a) Evolution of the pore diameters estimated by gas-flow porometry and (b) evolution of the relative radial PEM increment as a function of the number of bilayers for samples with an initial diameter of 100 nm and decrusted after each bilayer (orange squares) or decrusted every third bilayer (green triangles). Open symbols mean that the calculated gas flow was not constant during measurement.

Results for the 800 nm pore diameter are illustrated in figure 4.4. The first observation is that the pore diameter of the pristine film is much smaller than what was

announced, 670 instead of 800 nm. It can be seen in figure 4.4 **b** that the growth is linear and no regime transition is exhibited. The radial PEM increment does not reach 20% after the deposition of 9 bilayers, so the nanopores are far from being fully filled. For these samples the effect of the confinement is probably very low and the growth behavior is likely similar to that on a flat substrate.

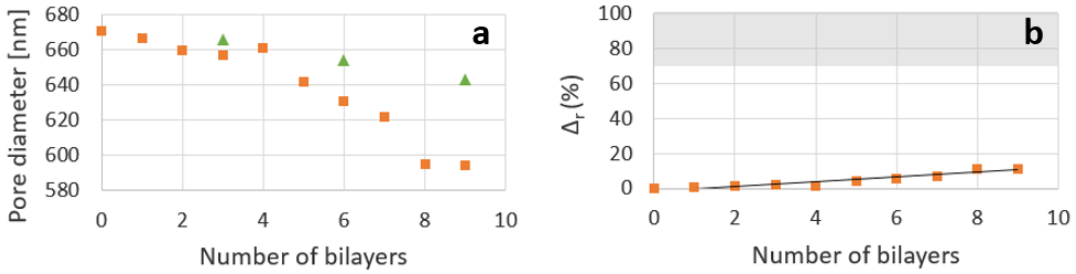

Figure 4.4 – (a) Evolution of the pore diameters estimated with gas-flow porometry and (b) evolution of the relative radial PEM increment as a function of the number of bilayers for samples with an initial diameter of 800 nm and decrusted after each bilayer (orange squares) or decrusted every third bilayer (green triangles).

The comparison of the final nanotube wall thickness after 8 bilayers (not 9 since the value for the 100 nm diameter pore is not reliable) for the different pore diameters indicates that the wall thickness of polymer nanotubes is strongly governed by the pore size of the template used. The total increments were 40.5, 101.5 and 38 nm for 100, 300 and 800 pore diameters respectively. The difference observed between the last two values is consistent with the literature: the growth increment is much larger in nanoporous templates than on flat substrates as large pores with a diameter of 800 nm can be considered.[4] The same comparison with a flat substrate can not be done with the smallest pore diameter since the pores are very quickly filled and PEM growth is thus very limited. However if the first three layers are considered, the pore thickness increment is again much larger for small pores where the confinement is important than for large pores viewed as flat substrates.

4.1.2 Observation of the PC membrane

In order to analyze the effect of the decrusting on the PEM film that is formed on the top and bottom surfaces of the PC template, three PC membranes with an initial pore diameter of 300 nm were imaged by SEM: a pristine membrane (figure 4.5 **a**), a membrane after the deposition of 9 bilayers and decrusted after each bilayer (figure 4.5 **b**) and a membrane after the deposition of 9 bilayers and decrusted only at the end of the deposition (figure 4.5 **c**). As expected, the pristine membrane is a smooth surface with randomly distributed pores which have a regular shape with a diameter of more or less 300 nm. Some of them merged in larger pores and will create nanotubes with a larger outer diameter.

For the second sample, with the deposition of 9 bilayers and a regular decrusting, the pores appear with a less regular shape. Furthermore most of them seem clogged even if the entrance of the pore is still visible with a pore diameter close to 300 nm. However, according to the porometry measurements, pores should have an average diameter of 84

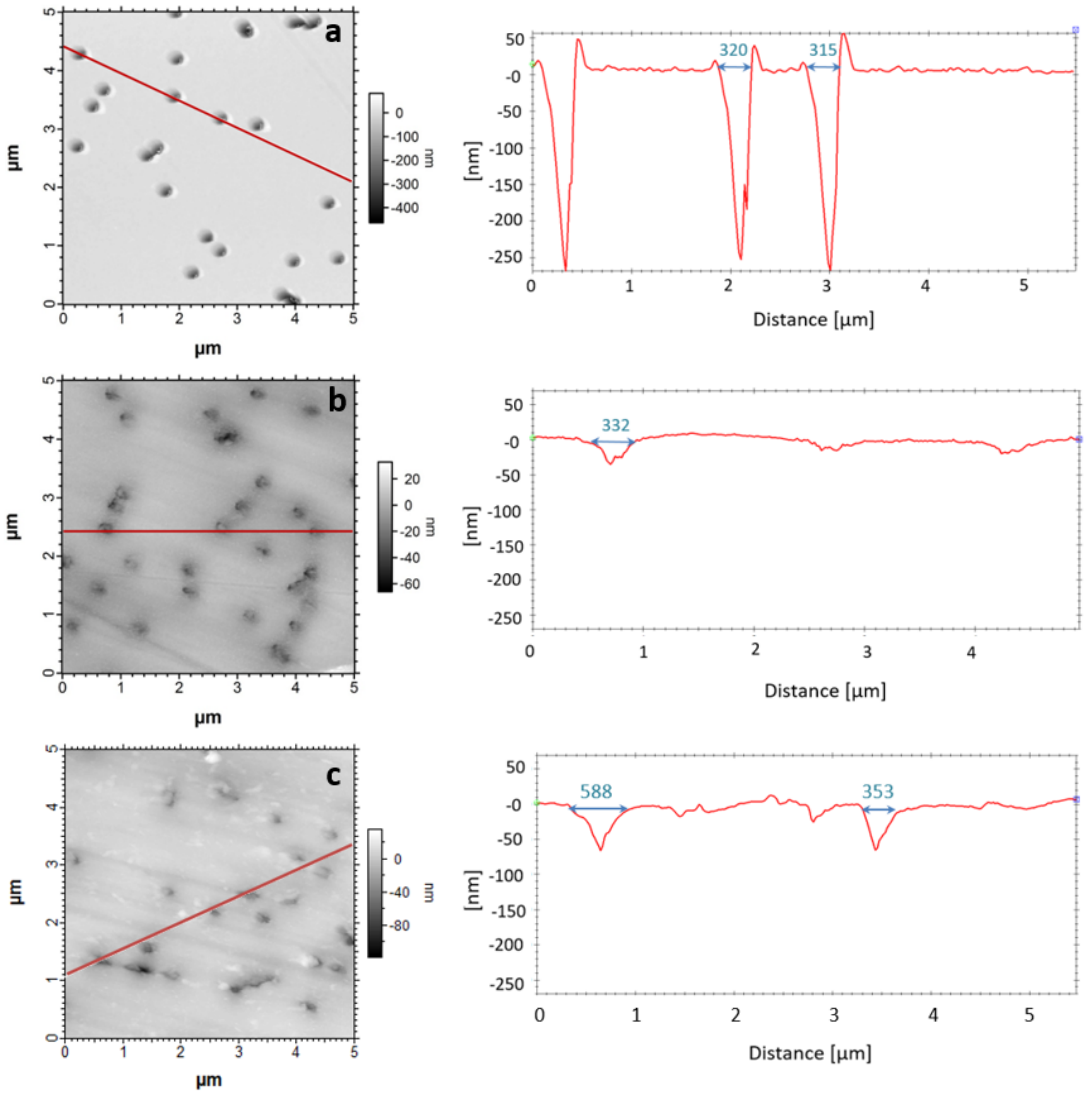

Figure 4.5 – SEM images of (a) a pristine PC membrane, (b) a PC membrane after the deposition of 9 bilayers and a decrusting after each bilayer and (c) a PC membrane after the deposition of 9 bilayers and a decrusting at the end of the assembly with the corresponding section profile marked by a red line the images.

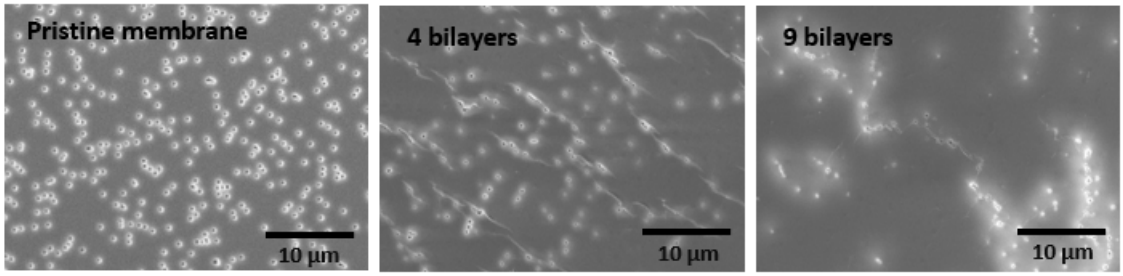

Figure 4.6 – SEM images of a pristine PC membrane, a PC membrane after the deposition of 4 bilayers and a PC membrane after the deposition of 9 bilayers which were decrusted after each bilayer.

nm. That means that this value is an average of clogged pores and larger pores and that pore diameter is not as well controlled as porometry measurements could suggest. Between the pores, the surface looks smooth which means that the regular decrusting is efficient. The lines through the image indicates the orientation of the decrusting.

For the last sample, which has been decrusted only once, the surface is rougher and a lot of small lighter spots are observed on it. Therefore one decrusting does not allow to remove the entire polymer film that is formed on the top and bottom surfaces of the template. Once again, some lines through the image point out the direction of the decrusting. In this sample, the pore shape is still less regular than for the previous one. A lot of pores also seem clogged while, according to porometry, they should have an average pore diameter around 169 nm. This shows again that the control of the pore diameter is not very precise.

SEM analysis of the PC surface of samples decrusted after each bilayer, illustrated in figure 4.6, indicates that pore density decreases with the number of bilayers. So even a regular decrusting does not avoid pore clogging which increases with the number of bilayers.

4.1.3 Morphology and rigidity of PAH/PSS nanotubes

Dependence on the number of bilayers

After a releasing step of the nanotubes from the template, their imaging by SEM gives some information about the morphology and the rigidity of the nanotubes depending on the number of bilayers. Figure 4.7 displays SEM images for nanotubes with a theoretical outer diameter of 300 nm after the deposition of 3, 4, 5, 6 and 9 bilayers. These nanotubes have been decrusted after each bilayer. This selection of samples has been made on the basis of the porometry results (figure 4.1). Samples from 3 to 6 bilayers have the biggest thickness increment and they are thus more likely to show the growth evolution of the nanotube with the number of bilayers. Whereas nanotubes with 9 bilayers are also analyzed to verify whether there is a difference with 6 bilayers samples although they have the same wall thickness according to the porometry. From the SEM image of nanotubes with 3 bilayers, it is not possible to highlight well defined nanotubes: a filamentous network is observed but nanotubes do not have two defined ends. The deposition of 3 bilayers is thus not enough to get mechanically stable nanotubes after membrane dissolution. For all the other samples, SEM images show that all nanotubes have a length slightly lower than 25 μm which corresponds to PC membrane thickness. The average values on 30 nanotubes were 23.7, 24.8, 23.7 and 22.3 μm for 4, 5, 6 and 9 bilayers respectively. Although there are imprecisions due to the measurement method, it can be supposed that the regular decrusting slightly damages the pore entrances and reduces nanotube length. About the nanotube outer diameter, figure 4.7 **f** points out that even with 9 bilayers, a lot a nanotubes have an outer diameter considerably lower that the template pore diameter what would suggest a collapse of the nanotube walls after releasing. Furthermore the diameter is not constant all along the nanotube axis; the nanotube ends are often wider as seen in figure 4.7 **f**. The control of the diameter is thus not as easy as template method would theoretically suggest. In addition, a lot of nanotubes are still linked to each other which means that the decrusting does not allow to dissociate all pore entrances.

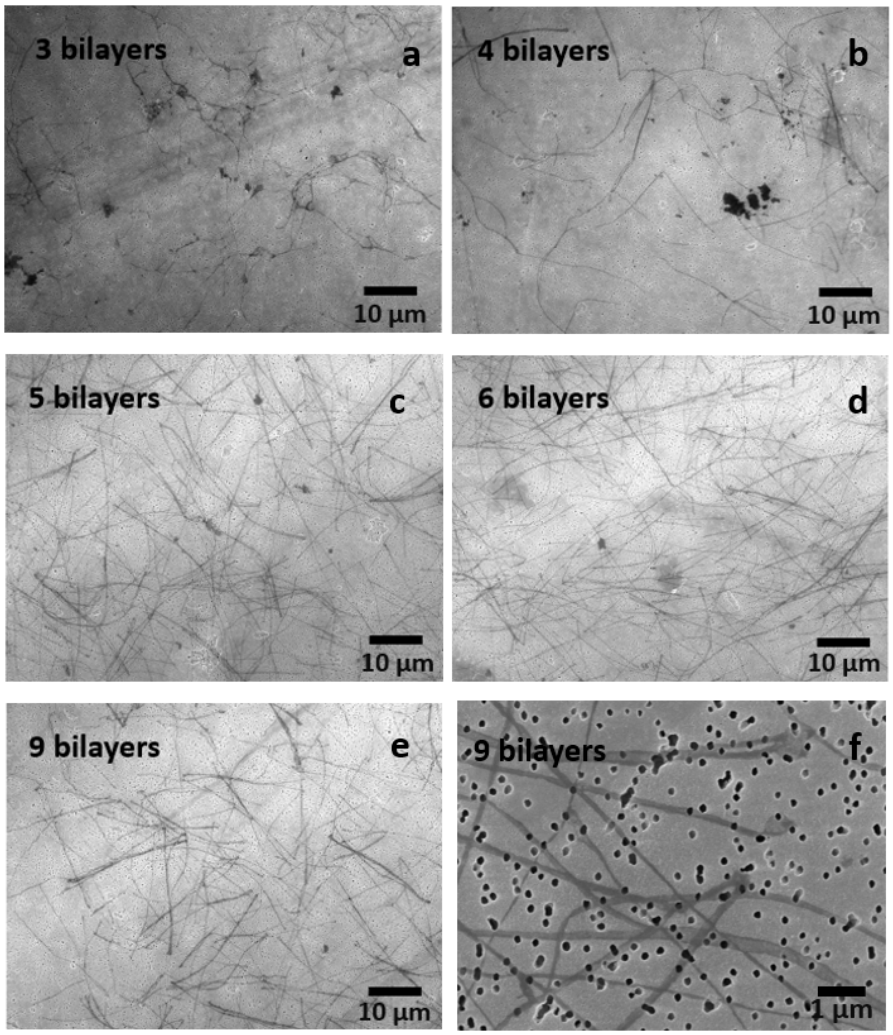

Figure 4.7 – SEM images of nanotubes with a diameter of 300 nm after the deposition of 3, 4, 5, 6 and 9 bilayers and which have been decrusted after each bilayer.

The results for persistence length and Young's modulus of the nanotubes are presented in table 4.1. First, by comparing the ratio r which quantifies the flexibility of the nanotubes (defined in section 3.3), it can be seen that the rigidity of the nanotube increases with the number of bilayers until 6 bilayers. The thickness increment for each bilayer makes thus nanotubes more rigid. Between 6 and 9 bilayers, the difference of rigidity is very small. This is consistent with porometry results (figure 4.1) which show that growth increment between these two samples is almost zero, so both samples should be morphologically very similar and have the same mechanical properties.

The Young's modulus calculated from the persistence length and the second moment of inertia according to the equation 3.6 is much smaller than what was expected. In the literature, Young's modulus of freestanding PAH/PSS capsules have been found in the range of 200-400 MPa by colloidal probe AFM force spectroscopy and by capsule

Number of bilayers	$r = \frac{R_{EE}^2}{L^2}$ **[-]**	r_0 **[nm]**	r_i **[nm]**	I **[m^4]**	L_p **[nm]**	E **[Pa]**
4	0.810	137.5	113.5	$1.50 * 10^{-28}$	9608	259
5	0.904	137.5	73	$2.58 * 10^{-28}$	11229	176
6	0.976	137.5	39	$2.79 * 10^{-28}$	11550	167
9	0.962	137.5	41.5	$2.78 * 10^{-28}$	10746	156

Table 4.1 – Measurement of the ratio $r = \frac{R_{EE}^2}{L^2}$, the persistence length, L_p, and the Young's modulus, E, for nanotubes with a diameter of 300 nm after the deposition of 3, 4, 5, 6 and 9 bilayers and which have been decrusted after each bilayer.

swelling.[24, 34] The small values obtained call into question the validity of the equation used to calculate E in the particular case of this system. In order to have a larger value for E, there should be a second contribution, X, besides the temperature, at the origin of the nanotube flexibility, i.e., we should have the following equation

$$E = \frac{L_p(k_B T + X)}{I}$$

with X an energy which is very large to increase E. This additional contribution could, for example, come from the forces exerted by the substrate on the nanotubes.

Finally it can also be noted that, even if Young's modulus values for all samples are in the same range of values, E is not constant as it should be since it is an intrinsic property of the material. The reason is that the moment of inertia increases faster than the persistence length for an increasing number of bilayers (except for 9 bilayers) so the Young's modulus decreases. This variation of E should come from the accumulation of inaccuracies from both the porometry and persistence length measurements.

Dependence on the template pore diameter

The influence of template pore diameter on the nanotube rigidity is studied for a number of bilayers set at 6 bilayers and a decrusting after 3 and 6 bilayers. SEM images for template pore diameter of 100, 300 and 800 nm are illustrated in figure 4.8. For the first sample (100 nm), nanotubes are too flexible and too entwined to enable measurement of the nanotube length. It is therefore not possible to quantify their rigidity but it is obvious, from the SEM images, that they are less rigid than nanotubes from the other two samples. For the other two samples, the nanotube length is slightly smaller than template pore length as already observed in the last section. The average values on 30 nanotubes were 24.3 instead of 25 μm for 300 nm pore diameter and 23.1 instead of 24 μm for 800 nm pore diameter. SEM images also indicate that, although the nanotube outer diameter increases with template pore diameter, there are both very different after nanotube release. Indeed nanotube outer diameter of the three samples is very variable and, very often, considerably smaller than template diameter.

The results for persistence length and Young's modulus are presented in table 4.2. By comparing the ratio r, it clearly appears that the nanotubes with the largest outer diameter are more rigid. This result is coherent with equation 3.6 for a constant Young's

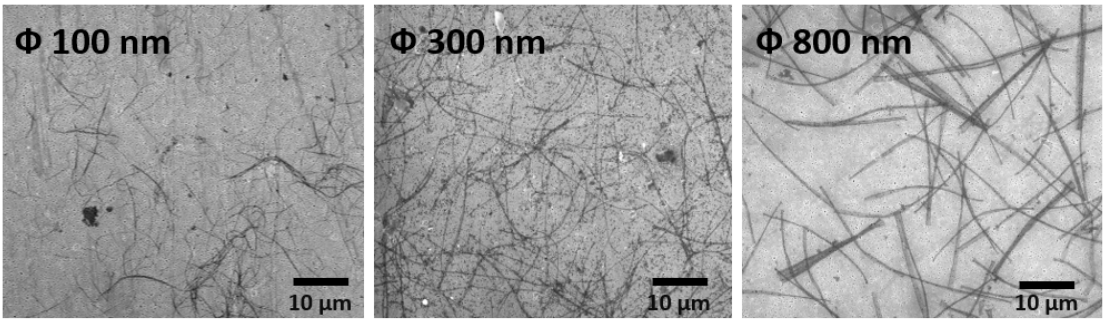

Figure 4.8 – SEM images of nanotubes with an outer diameter of 100, 300 and 800 nm after the deposition of 6 bilayers and which have been decrusted after 3 and 6 bilayers.

Pore diameter [nm]	$r = \frac{R_{EE}^2}{L^2}$ **[-]**	r_0 **[nm]**	r_i **[nm]**	I **[m^4]**	L_p **[nm]**	E **[Pa]**
300	0.787	137.5	62.5	$2.69 * 10^{-28}$	9559	144
800	0.961	335.5	327	$9,71 * 10^{-28}$	11112	46

Table 4.2 – Measurement of the ratio $\frac{R_{EE}^2}{L^2}$, the persistence length, L_p, and the Young's modulus, E, for nanotubes with a diameter of 100, 300 and 800 nm after the deposition of 6 bilayers and which have been decrusted after 3 and 6 bilayers.

modulus. Indeed, although the wall thickness is much smaller for the largest outer diameter (8.5 nm compared with 75 nm), its inertia is much greater, therefore the persistence length should be longer and the nanotubes should be more rigid.

4.2 Characterization of the mats

On the basis of the results from the previous chapter, we chose to build mats from nanotubes with 6 bilayers which are decrusted every third bilayer, except where noted. The deposition of 6 bilayers provides nanotubes which are mechanically stable enough and it is not necessary to add more layers since the thickness increment after 6 bilayers is very weak. In addition, to optimize the work we have seen that a decrease of decrusting frequency to every third layers was enough to limit crusting to the same extent as a decrusting after each bilayer.

4.2.1 Morphological characterization, influence of water and variation of the number of bilayers

Before studying the influence of some processing parameters on mat build-up, the first characterization step was to analyze the general morphology of a mat by SEM and AFM. Results for a mat with 9 (only exception to what was stated in the previous paragraph) bilayers nanotubes decrusted every third bilayer are shown in figures 4.9 and 4.10. It can be seen in these images that nanotubes constituting the mat look like a network of very entwined fibers with a lightly rough outer surface. Nanotubes are still clearly observable and have kept their integrity although some parts seem to have merged and result in smoother areas. These images also show that the porosity in the mat is high

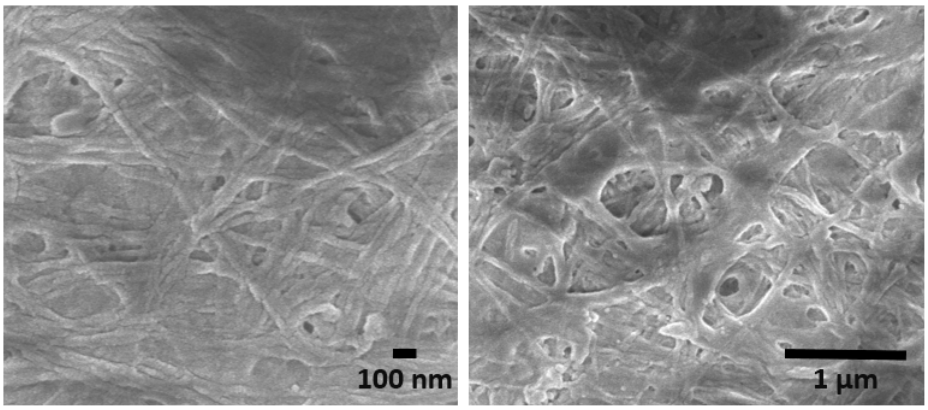

Figure 4.9 – SEM images of a mat made of nanotubes with 9 bilayers.

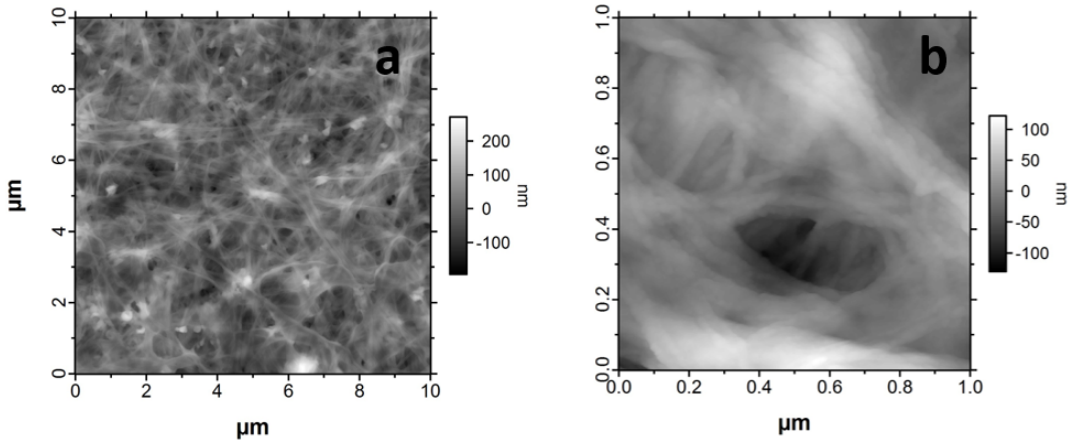

Figure 4.10 – AFM images of a mat of nanotubes with 9 bilayers.

with some deep pores that penetrate in the layer over more than several hundreds of nanometers. The observation of nanotubes and presence of porosity suggests that the compressive forces induced by the filtration step during the mat build-up are not too large and do not crush nanotubes on the PET membrane. Some points are a little bit higher in the mat (white points in figure 4.10 **a**). According to their size, these points could correspond to the larger nanotube extremities already observed in section 4.1.3 which, being larger, exceed the top surface. In some areas, the AFM image of the sample with 9 bilayers looks like the mat is covered by a smooth film. This effect is very likely not caused by a tip effect from the AFM but its nature is still not explained. A first hypothesis is that it is an agglomerate of undissolved PC template. The presence of undissolved PC on the surface layer of the mat was checked by ToF-SIMS as described in section 4.2.2. Although ToF-SIMS analysis proved that undissolved PC is still present on the mat, it can not be related to the films observed by AFM. A second hypothesis is a deposit of non adsorbed PAH and PSS that form a film.

Subsequently the mat morphology was studied for two different parameters: number of bilayers and humidity of environment after build-up. Their effects are presented in figures 4.11 and 4.12 for two different magnifications. The morphology of all these

samples is similar to what was observed and described in the above paragraph. The influence of the number of bilayers on the nanotube morphology was observed in section 4.1.3 and the conclusion was that rigidity of nanotubes increases with the number of bilayers until 6 bilayers. After the deposition of 6 bilayers, the increment of thickness is so small that there is no difference of rigidity. This is also what figures 4.11 and 4.12 indicate. Nanotubes have a longer persistence length and are thus more rigid in the sample with 6 bilayers compared to the sample with 3 bilayers, and no significant differences are observed between 6 and 9 bilayers as expected. About mat porosity, it could be assumed that porosity of the mat is related to nanotube rigidity. However the simple observation of AFM images does not allow to check this assumption. To do such a study, the samples could be analyzed by capillary flow porometry, as it was carried out by Li et al. to characterize nanofibrous membranes prepared by electrospinning.[35]

Regarding the influence of humidity, a comparison is made between two degrees of humidity: humidity of the ambient air and 100% humidity in water. As explained in section 2.7.1, a difference of swelling of about 30% is expected for flat PEMs between these two environments. However, in the present case of mats with nanotubes, the swelling induced by humidity is influenced by the tubular structure. Therefore the difference of swelling between the two environments for nanotube walls is probably slightly different from 30%. Indeed since the structure is tubular, there are several additional contributions to take into account: due to swelling, the inner part of the tube will undergo compression, the outer part will undergo traction and confinement will also induce stresses since, in solution, the central part of the tube is almost closed. The swelling of a flat substrate with identical thickness to the nanotube, 75 nm in this case, should induce a thickness increment of almost 25 nm. This value is thus an estimation of what should be observed for nanotube walls. However, pixel size of images 4.11 and 4.12 does not allow to measure a so small thickness increment and observe swelling.

4.2.2 Presence of PC

For the mat build-up, nanotubes are first released from the PC template by dissolution in CH_2Cl_2. Although PC is very soluble in CH_2Cl_2, it can be suspected that some traces are still present in the mat after the build-up. To check the presence of PC on mats, ToF-SIMS characterization technique has been applied to three mats composed of nanotubes with 3, 6 and 9 bilayers. The three mats have been made with the same quantity of nanotubes using the same area of PC membrane. The main PC characteristic peaks in ToF-SIMS spectra are in the negative ion spectrum and correspond to mass-to-charge ratios equal to 211 ($C_{14}H_{11}O_2^{-1}$), 133 ($C_9H_9O^{-1}$) and 117 ($C_8H_5O^{-1}$) m/z. Results for the range from 203 to 252 m/z are illustrated in figure 4.13. These partial spectra show that the 211 peak is present for all samples. Therefore there is residual PC in the three samples which means that the template does not dissolve entirely during the nanotube releasing. This element will have to be taken into account for future applications, especially if these are biological applications. A quantitative analysis of these results is however difficult due to the strong variation of the ionisation yield which depends on a lot of parameters. Nevertheless, relative quantitative information can be derived from a spectrum comparison or by computing intensity ratios. The ratios of the intensity of the 211 peak over the total intensity are $5.38 * 10^{-3}$, $3.95 * 10^{-3}$ and $7.29 * 10^{-3}$ for 3, 6 and 9 bilayers respectively. That suggests that PC is relatively more present in this last

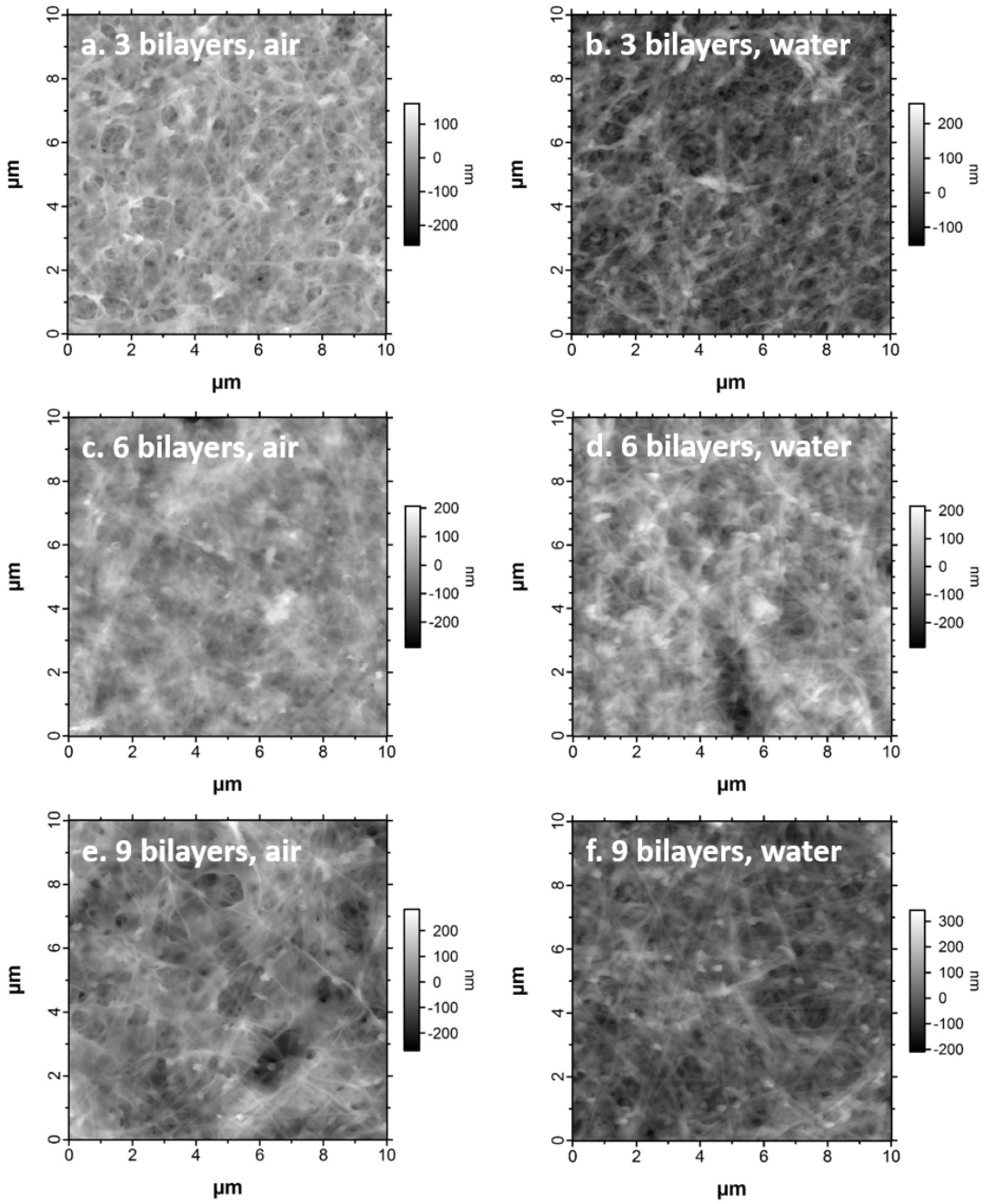

Figure 4.11 – AFM images of mats made of nanotubes with (a,b) 3, (c,d) 6 and (e,f) 9 bilayers in (a,c,e) air or in (b,d,f) water.

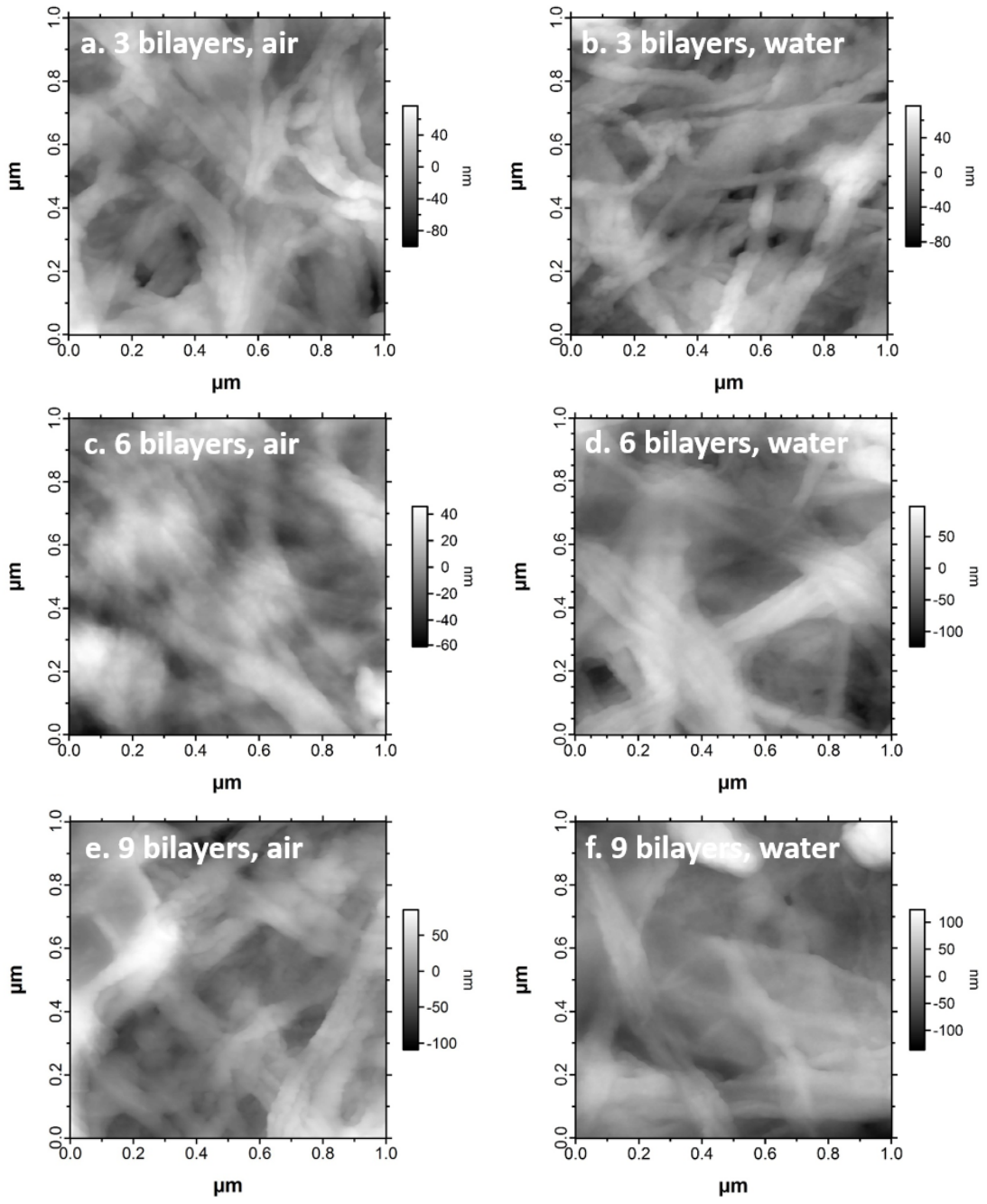

Figure 4.12 – AFM images of mats made of nanotubes with (a,b) 3, (c,d) 6 and (e,f) 9 bilayers in (a,c,e) air or in (b,d,f) water.

sample. However since the same quantity of PC was used in each sample, this difference could come from the sonication of the CH_2Cl_2 solution in which the PC template is dissolved, or could come from the rinsing steps during the filtration of the nanotubes.

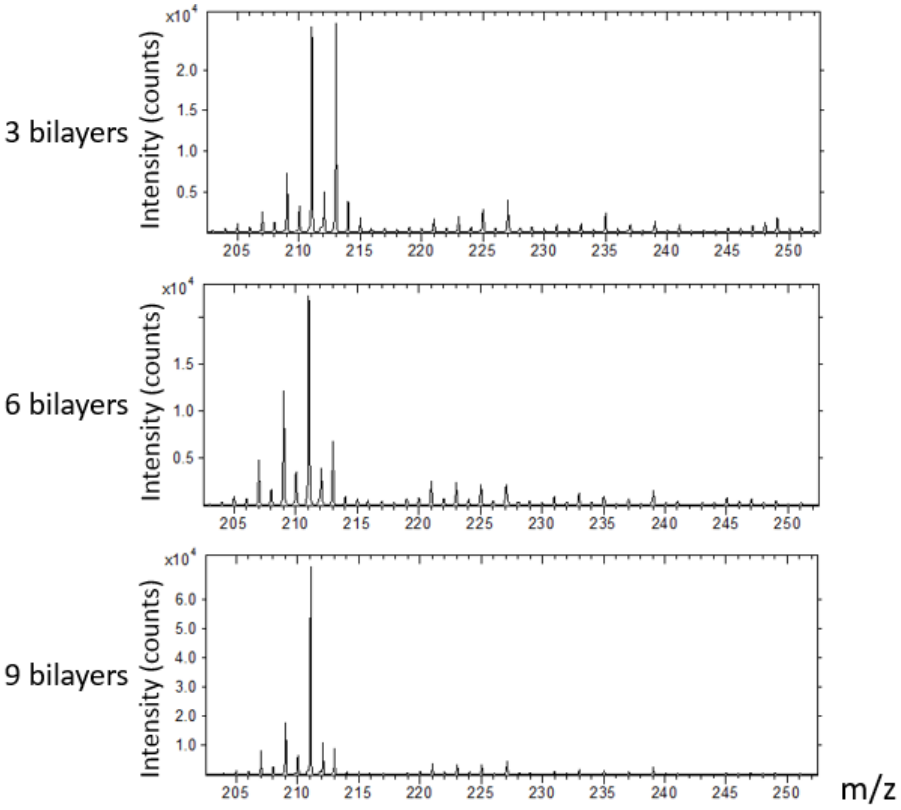

Figure 4.13 – Partial negative ion spectra from ToF-SIMS analysis for the mats with 3, 6 and 9 bilayers.

4.2.3 Variation of the nanotube area density

For the study of the influence of the number of nanotubes, four samples were prepared by dissolving four areas of PC membrane of varying size. The PC pore diameter was 300 nm. To get different quantities of nanotubes, the dissolved surface area of PC membrane was varied between 5 and 40 cm^2. Knowing the nanotube density in the template (1×10^8 pores·cm^{-2}) and the mat surface area (2.25 cm^2), the mat area density is calculated in table 4.3. In the rest of the text, each sample will be appointed by its number from table 4.3. Pictures of the four samples are in figure 4.14. Although it is not easy to distinguish the mat because of the light reflection on the gold layer, it is possible to observe a large whitish film for mats 3 and 4 while the two others are composed of small whitish areas which do not cover the whole mat area.

The mats were first imaged by fluorescence microscopy to analyze their lateral homogeneity (figure 4.16). As observed in figure 4.14, mats 1 and 2 do not form continuous films. For mat 1, nanotubes are scattered over the surface without forming any continuous areas. But the scattering is not perfect since the nanotubes seem to stick together

Sample number	Surface of the PC membrane [cm^2]	Area density [cm^{-2}]
1	5	$2.83 * 10^8$
2	10	$5.66 * 10^8$
3	20	$1.13 * 10^9$
4	40	$2.26 * 10^9$

Table 4.3 – Data of four mats of varying area density of nanotubes.

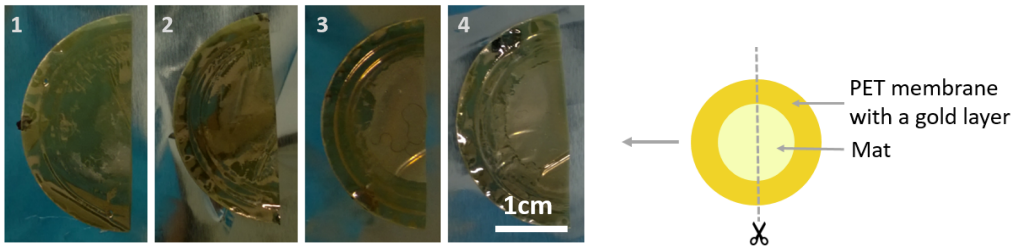

Figure 4.14 – Pictures of mat 1 to 4 with a corresponding scheme of the mat.

by gathering and leaving black areas. For mat 2 the nanotube density is higher; some continuous areas appear as shown in figure 4.16 **d**. Nevertheless there are still many totally black (uncovered) regions. The mat is thus absolutely not uniform over its whole surface. By increasing again the nanotube density, nanotubes finally fill all the gaps to form a continuous film (mats 3 and 4). Hence, there is a threshold density to get a continuous film, located between values of mats 2 and 3, $5.66 * 10^8$ and $1.13 * 10^9$ cm^{-2}. For mat 3, although the film is continuous, it is still not totally homogeneous. Indeed figures 4.16 **e** and **f**, which are representative of the whole surface, suggest that the mat build-up is in an intermediary phase where nanotubes either organize themselves in islets over a nanotube floor or are aggregates in the mat (figure 4.15).

Figure 4.15 – Assumptions about the structure of the mat in the intermediary phase where nanotubes either (a) organize themselves in islets over a nanotube floor or (b) are aggregates in the mat.

By doubling the nanotube density (figure 4.16 **g** and **h**), the islets disappear and the mat seems to become more homogeneous. That would suggest that once the entire surface is covered, the nanotubes first form small packets and then additional nanotubes fill the less dense areas rather than having a linear growth along the normal axis. Finally, fluorescence microscopy images have also revealed some cracks in the mats as seen in figure 4.17 for mat 4. These cracks are probably caused by folds in the underlying PET substrate. During the filtration step, the PET membrane is not perfectly flattened by

the pump on the filter, what is compounded by the partial swelling of PET in CH_2Cl_2. There are thus some fine folds in the PET membrane on which nanotubes sediment. Therefore during the sample preparation for fluorescence microscopy the flattening of these folds between the two glass slides probably creates some cracks.

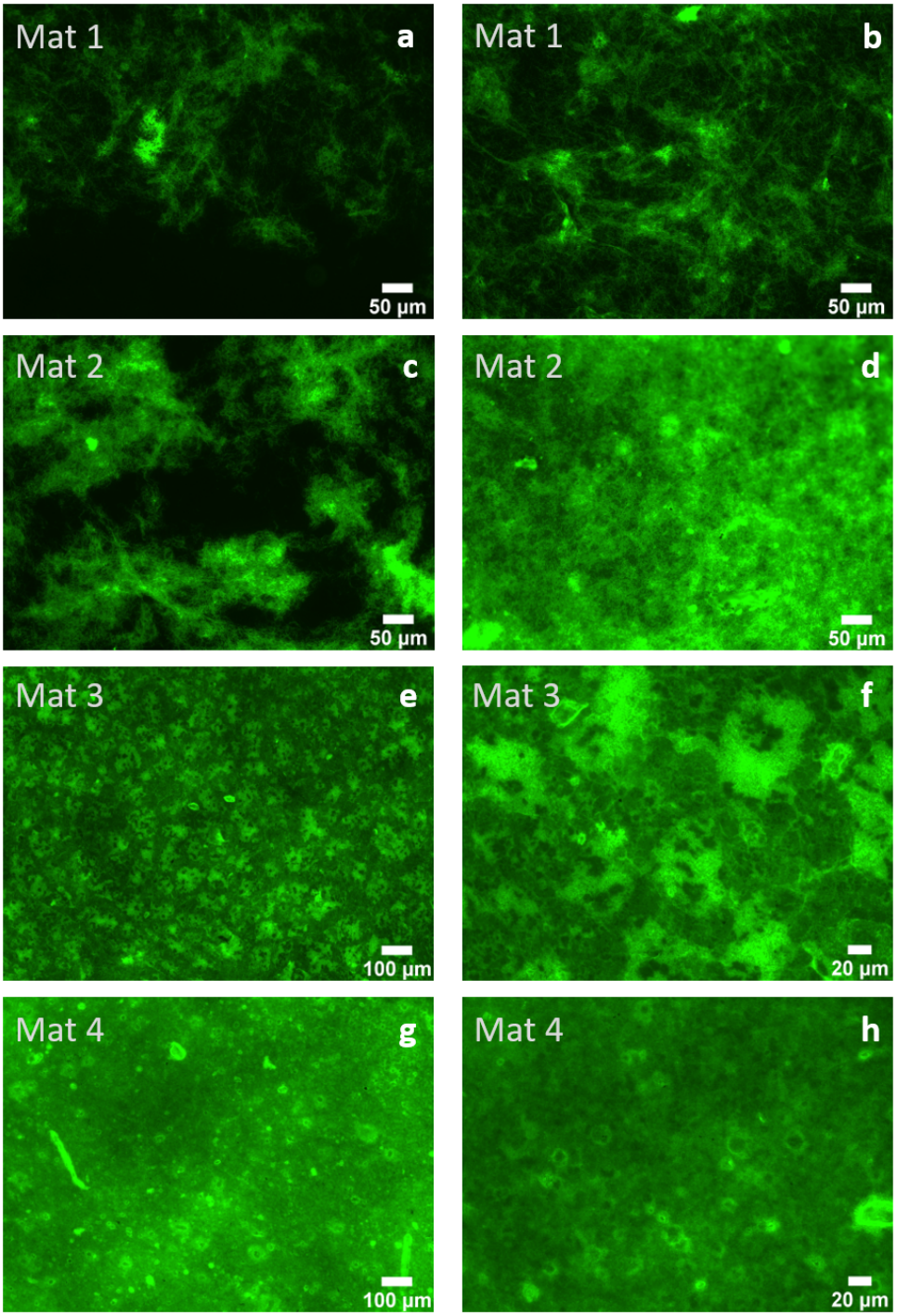

Figure 4.16 – Fluorescence microscopy images for mats 1 to 4.

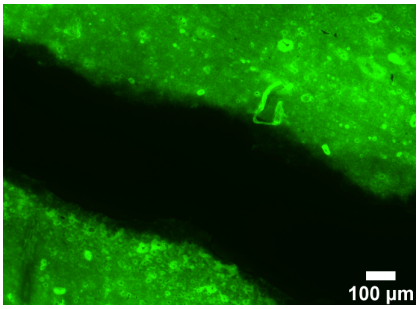

Figure 4.17 – Fluorescence microscopy image of a crack in mat 4.

Mats 3 and 4 were then observed by CLSM as shown in figure 4.18. The horizontal planes of these two samples are similar with what was observed by fluorescence microscopy. Indeed although the islets on mat 3 are not as clear as in figure 4.16, it can be seen that mat 3 is much more heterogeneous than mat 4. The cross-sections also indicate larger density fluctuations, and thus porosity fluctuations, in mat 3. However the thickness is relatively constant all along the section for both samples. Therefore, the islets previously observed are included within the mat and not resting over a nanotube layer. For each cross-section the side in contact with the substrate looks more diffuse. This effect could result from some nanotubes or unadsorbed materials that go inside the pores of the PET membrane. Some noise from the signal could also be added. Full width at half maximum of the mat cross-section of both samples, calculated as explained in section 3.5, are 9.09 and 6.82 μm for mat 3 and 4 respectively (figures 4.19 and 4.20). These values mean that the thickness is on the order of a few micrometers and does not increase with the number of nanotubes between mats 3 and 4. All these observations confirm that the growth begins by accumulating clusters, before extra nanotubes fill the less dense areas without significantly increasing the thickness, at least until the density value of mat 4.

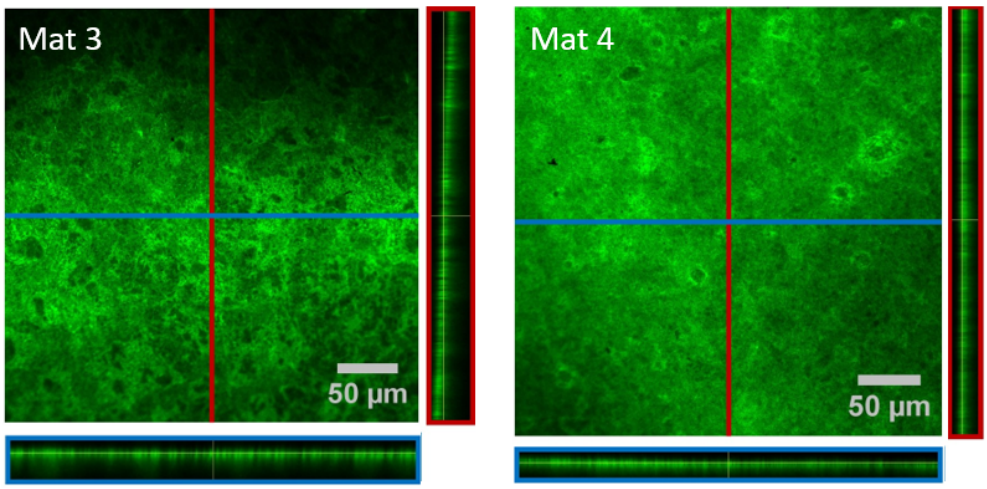

Figure 4.18 – CLSM images for mats 3 and 4. The images correspond to a plane of the z-stack (spacing of 1 μm) with two cross-sections performed along the red and blue lines. For the red sections the surface in contact with the substrate is on the right and for the blue sections the surface in contact with the substrate is at the bottom.

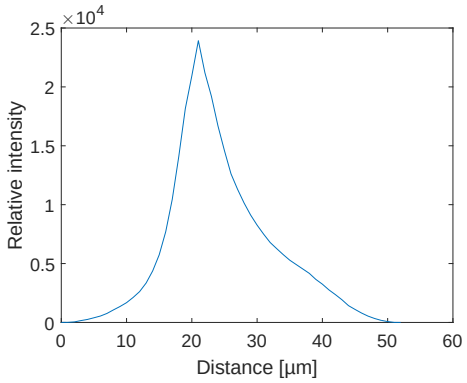

Figure 4.19 – Average profile of the cross-section of mat 3 imaged by CLSM.

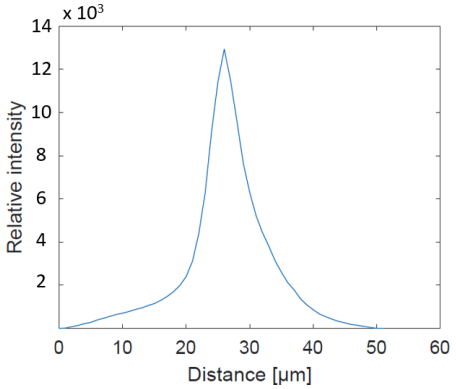

Figure 4.20 – Average profile of the cross-section of mat 4 imaged by CLSM.

In order to get a more precise value for the thickness, mat 4 was cut by cryomicrotomy and observed by optical microscopy. It is important to note that, during the preparation, the sample was in contact with water which causes mat swelling. In figure 4.21, the porous PET membrane and the mat are clearly observable with a gold layer between them. With this method the measured thickness is close to 1 μm which is significantly lower than the approximation measured from CLSM. Although CLSM only gives an approximation, it is reasonable to think that the mat is thicker than 1 μm. An hypothesis for the low value from optical microscopy is that the sample preparation might have damaged the sample by crushing the soft mat during the cutting step. To avoid this, another sample was prepared by fixing it in an epoxy resin but the mat did not resist the cut and was torn under the strain as seen in figure 4.22.

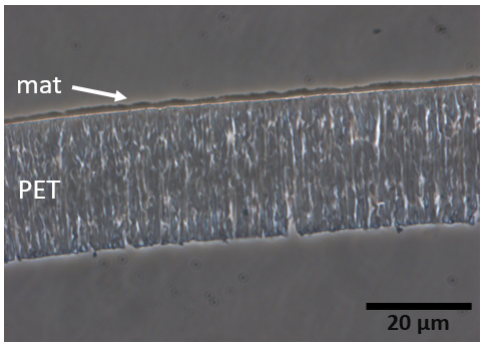

Figure 4.21 – Optical microscopy image of mat 4. The sample was prepared by cryomicrotomy.

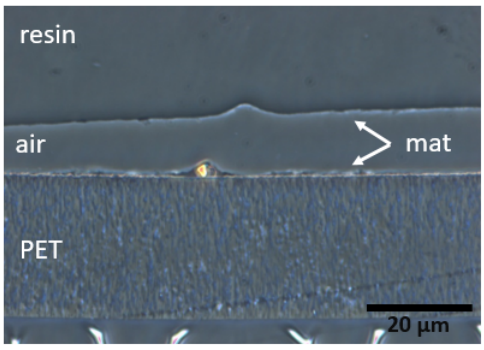

Figure 4.22 – Optical microscopy image of mat 4. The sample was first fixed in an epoxy resin and then cut by microtomy.

Mats 3 and 4 were also observed by AFM (figure 4.23). In order to compare the surface roughness of these two samples, which is linked to the surface porosity, AFM images were treated (Matlab R216a software) to obtain an histogram of the height. The RMS roughnesses of these histograms are 79 and 89 nm for mats 3 and 4 respectively. The difference of RMS roughness between these two samples is thus in the range of 10 nm, which is not significant for the AFM study of this system. This analysis was repeated for two other areas where the RMS roughnesses were 85 and 80 nm for mats 3 and 4 respectively. The comparison of these two values leads again to the same conclusion, i.e., the addition of nanotubes does not modify the surface roughness and thus the surface porosity. However it should be kept in mind that these samples are quite heterogeneous, therefore a study on much broader areas would be interesting.

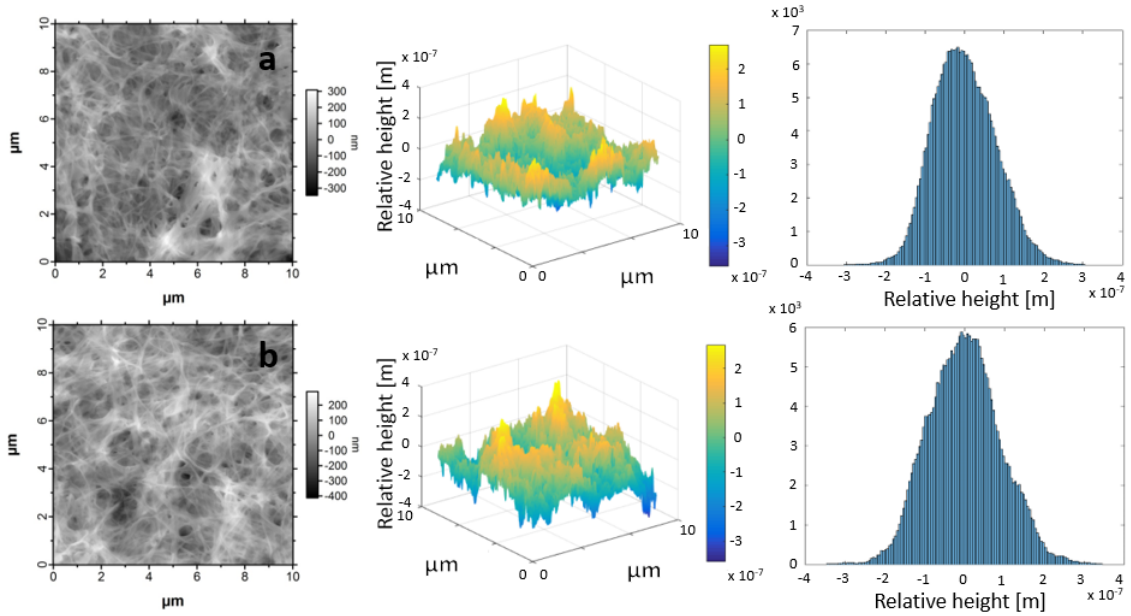

Figure 4.23 – Matlab analysis (3D plot and histogram) of AFM images of (a) mat 3 and (b) mat 4.

On the basis of the results of this section, the next mats will be prepared with the same area density as mat 4, which is $2.26 * 10^9$ cm^{-2}, to ensure that mats are continuous and homogeneous.

4.2.4 Variation of the nanotube diameter

To study the influence of the nanotube diameter on the mat morphology, the results for mat 4 from the previous section, which is made of nanotubes with a diameter of 300 nm, are compared with two other samples having the same nanotube density ($2.26*10^9$ cm^{-2}) but nanotube diameters of 100 and 800 nm. It is worth noting that these diameters are the theoretical outer diameters corresponding to the template pore diameters. Results of the fluorescence microscopy analysis for the diameters of 100 and 800 nm are presented in figure 4.24. By comparison with figures 4.16 **g** and **h**, the mats with nanotubes with diameters of 100 and 300 nm look similar, they are both quite homogeneous and show a few impurities. By contrast, the images of the mat with the largest nanotubes are different and show some specific structures, which look filamentous, distributed over the whole sample. Because of the size of these structures, it is not possible that the filamentous aspect is due to the nanotubes. Currently, we do not have any hypothesis to explain this particular morphology. Since these structures were only observed on one sample, complementary investigations are required.

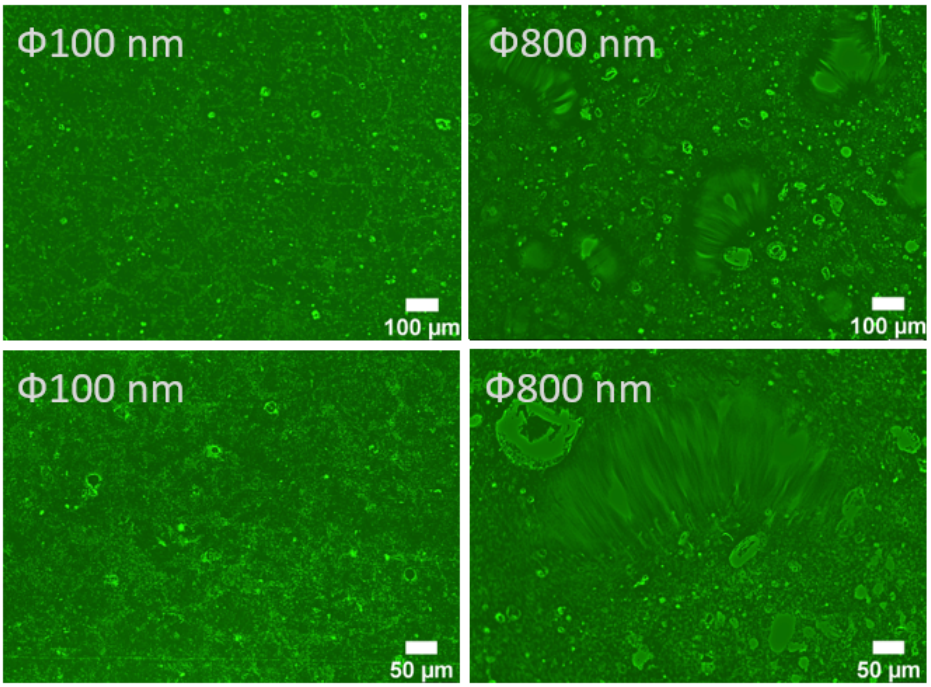

Figure 4.24 – Fluorescence microscopy images for mats made of nanotubes with a diameter of 100 and 800 nm.

To compare relatively the thickness of these three mats, CLSM images of the cross-sections (figure 4.25) have been processed in the same way as in the previous section. The full widths at half maximum of these mats are 4.78, 6.82 and 9.53 μm for diameters of 100, 300 and 800 nm respectively (figure 4.20 for 300 nm and figures 4.26 and 4.27 for 100 and 800 nm). As expected, the larger the diameter is, the thicker the corresponding mat is.

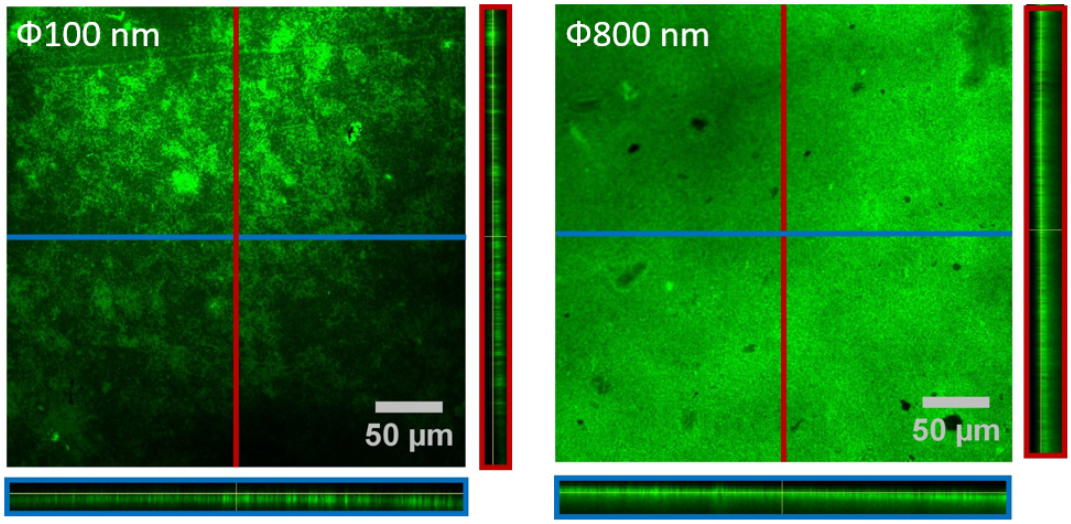

Figure 4.25 – CLSM images for mats made of nanotubes with a diameter of 100 and 800 nm. The images correspond to a plane of the z-stack (spacing of 1 μm) with two cross-sections performed along the red and blue lines. For the red sections the surface in contact with the substrate is on the right and for the blue sections the surface in contact with the substrate at the bottom.

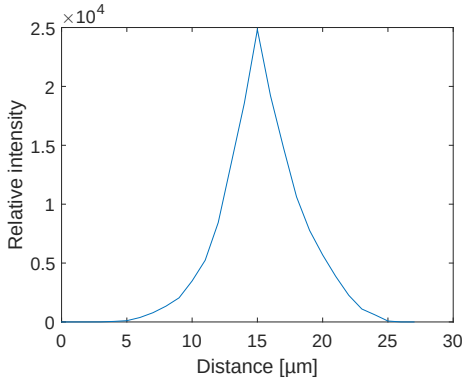

Figure 4.26 – Average profile of the cross-section of the mat made of nanotubes with a diameter of 100 nm imaged by CLSM.

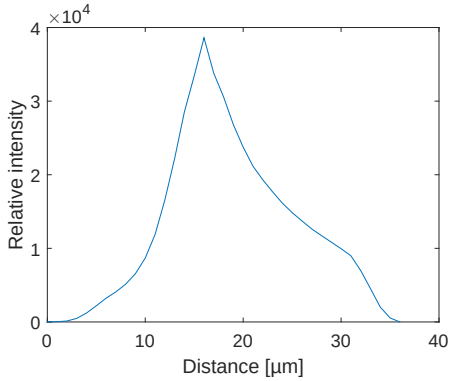

Figure 4.27 – Average profile of the cross-section of the mat made of nanotubes with a diameter of 800 nm imaged by CLSM.

Finally the three samples were observed by AFM to compare their surface roughness (figure 4.28). AFM images were again treated to obtain histograms of the height. The RMS roughnesses of these histograms are 35, 80 and 92 nm for diameters of 100, 300 and 800 nm respectively. The larger the diameter is, the rougher the surface is, which also means that the porosity at the surface is higher. This conclusion is confirmed by Li et al.[35] who studied the effect of fiber diameter on the pore size and pore size distribution of nanofibrous membranes obtained by electrospinning. They concluded that the fiber

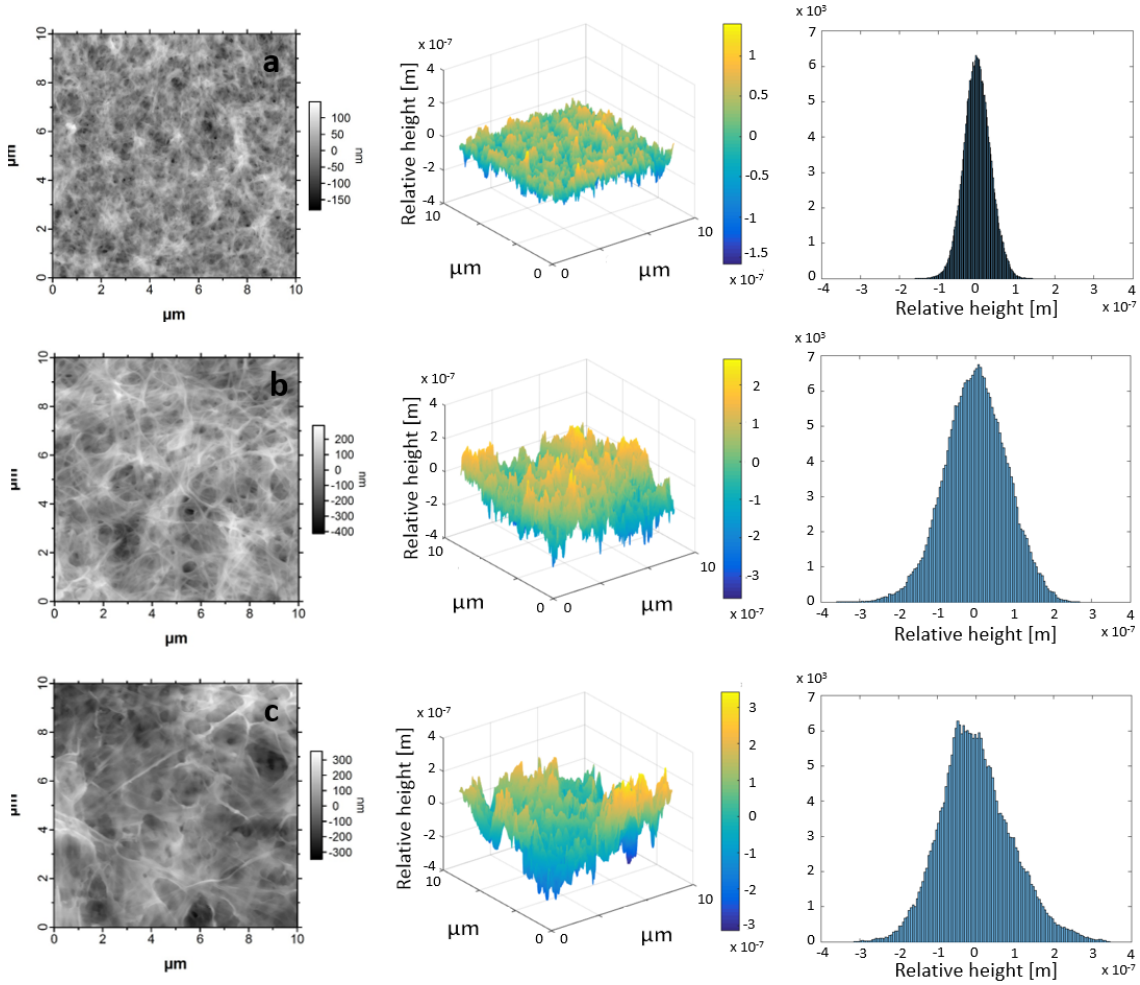

Figure 4.28 – Matlab analysis (3D plot and histogram) of AFM images of mats made of nanotubes with a diameter of (a) 100, (b) 300 and (c) 800 nm.

diameter was a dominant factor in determining the porosity of the fibrous membrane and also observed that decreasing the fiber diameter decreases the pore size for samples of constant mass.

4.2.5 Young's modulus

In order to measure the Young's modulus of a mat made of PAH/PSS nanotubes, the force spectroscopy mode of AFM was applied on mat 4 from section 4.2.3. This is thus a mat made of nanotubes with 6 bilayers and a theoretical outer diameter of 300 nm. To scan an area covering a lot of nanotubes at the same time and get a value for the mat and not for one nanotube, sensors with integrated colloidal particles with a diameter of several micrometers were used to indent the samples. When samples are imaged with these tips, the observed morphology looks like figure 4.29. Since colloidal particles scan a larger area for each point, the morphology is dilated by the shape of the colloid: the colloid is imaged by the surface, rather that the reverse.

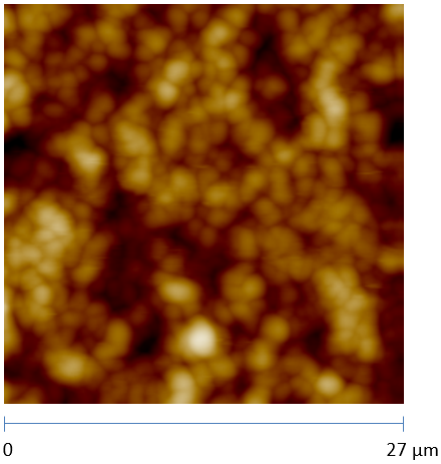

Figure 4.29 – AFM image of the mat using a sensor with an integrated colloidal particle of 5 μm diameter.

Trig threshold [nN]	Contact stiffness, k_N [N/m]	Average Young's modulus, E [MPa]
150	43.12	106
300	63.62	134
450	63.61	109

Table 4.4 – Contact stiffness and Young's modulus of the mat as a function of the trig threshold measured by AFM with a cantilever having a stiffness constant equal to 2.94 N/m.

The distribution of the Young's modulus value obtained with a first cantilever ($k =$ 2.94 N/m) is displayed in figure 4.30 as a function of the "trig threshold" which is the force applied to the sample. The larger the force is, the larger the scanned thickness is. Average values for each trig threshold, in table 4.4, are in the same range. Furthermore these values are close to the values in the literature for PAH/PSS multilayers (200-400 MPa as seen in section 4.1.3). The Young's modulus of the mat and of the nanotubes can obvisouly not be directly compared with each other since the modulus of the mat depends on several morphological parameters such as the number of nanotubes per unit area or the number, the type and the position of the junctions between nanotubes. Nevertheless the properties of the nanotubes and the mat should be proportional, i.e., the more rigid the nanotubes are, the more rigid the mat should be. And since both Young's modulus are close to each other, this suggests that the proportionality factor between them is close to one.

On the basis of these results, the contact stiffness has been calculated according to equation 3.12 and has an average value of 57 N/m. Since the stiffness constant of the cantilever is much lower than this value, that means that the scanned thickness was very thin and maybe not representative of the bulk. Therefore the experiment was repeated with a sensor having a stiffness constant closer to the contact stiffness. The second cantilever had a stiffness constant of 53.6 N/m. The Young's modulus distribution for a trig threshold of 150 nN is illustrated in figure 4.31. This graph presents a very large distribution and suggests that the method is not adapted to measure the Young's

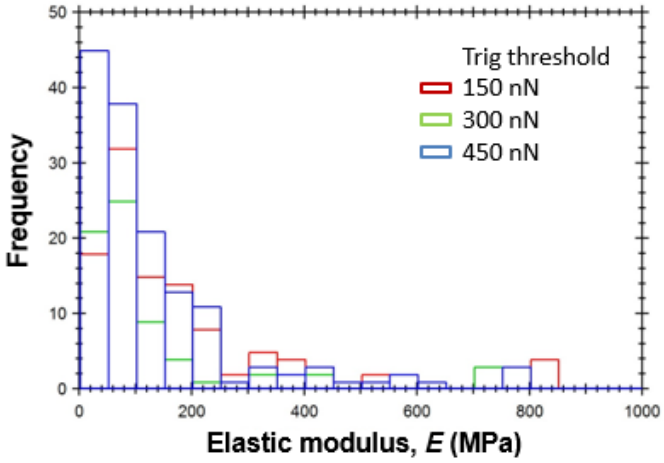

Figure 4.30 – Distribution of the Young's modulus as a function of the trig threshold. The measurement was performed with a cantilever having a stiffness constant equal to 2.94 N/m.

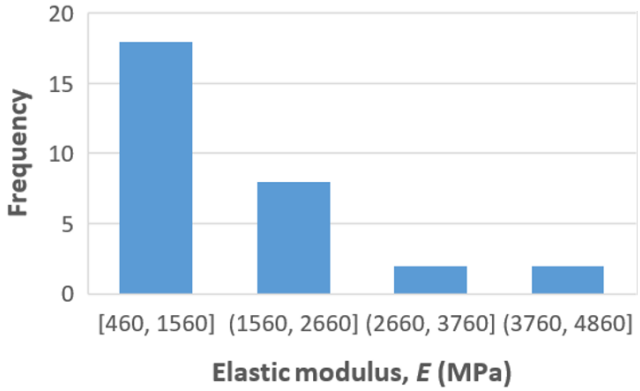

Figure 4.31 – Distribution of the Young's modulus for a trig threshold of 150 nN. The measurement was performed with a cantilever having a stiffness constant equal to 53.6 N/m.

modulus. Furthermore the experiment was repeated several times in the same conditions and shows dramatically different results from one instance to the next. The experiment with this sensor is thus not reproducible. The reason of this difference between the two sensors with different stiffness constants is not explained yet. However, since a difference of stiffness constant induces a difference in the scanned thickness that means that the scanned thickness should be an important parameter to take into account.

4.2.6 Double mat

One of the targeted perspectives of the study is to develop self-standing mats comprised of different stacks of functional nanotubes by the repetition of filtration steps (scheme in figure 4.32). In this context and in order to verify that successive filtrations can lead to multilayered mats, a "double" mat has been fabricated by the successive filtration of PAH/PSS nanotubes with, first, one PAH-FITC labeled layer and subsequently nan-

otubes with one PAH-RITC labeled layer. The obtained double mat is imaged in figure 4.33, rosy appearance being due to the RITC label.

This double mat was first characterized by AFM in air. The observed surface morphology is shown in figure 4.34 and is similar to what was observed until now for mats consisting of nanotubes with 6 bilayers and a diameter of 300 nm (figure 4.23).

Figure 4.32 – Sketch of a double mat.

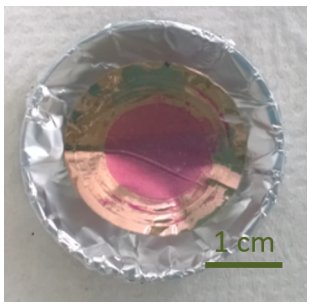

Figure 4.33 – Picture of the double mat.

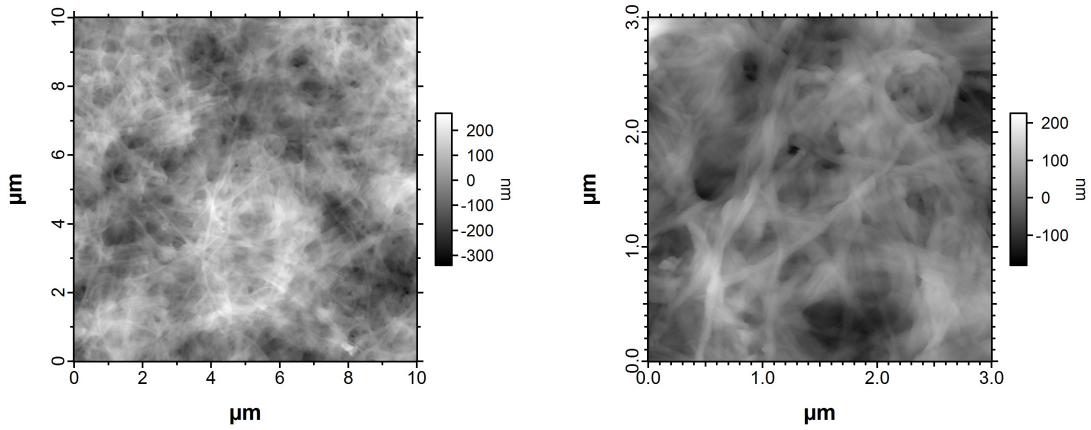

Figure 4.34 – AFM images of the double mat.

The mat was then imaged by fluorescence microscopy to highlight the presence of FITC labeled nanotubes which fluoresce in green (named green nanotubes) and RITC labeled nanotubes which fluoresce in red (named red nanotubes) (figure 4.35). These images indicate that both types of nanotubes form continuous layers which are homogeneous on the whole sample surface, with the exception of some red points observed on the combined image. These points suggest the presence of pores in the green layer that are filled with red nanotubes during the second filtration. Aside from these few pores, the red nanotubes are thus randomly distributed over the first mat. These images also show the presence of a few impurities.

The vertical distribution of green and red nanotubes in the mat thickness was highlighted by CLSM analysis in figures 4.36 and 4.37. The first figure corresponds to a plane section from the middle of the mat. The whole plane is composed of both green

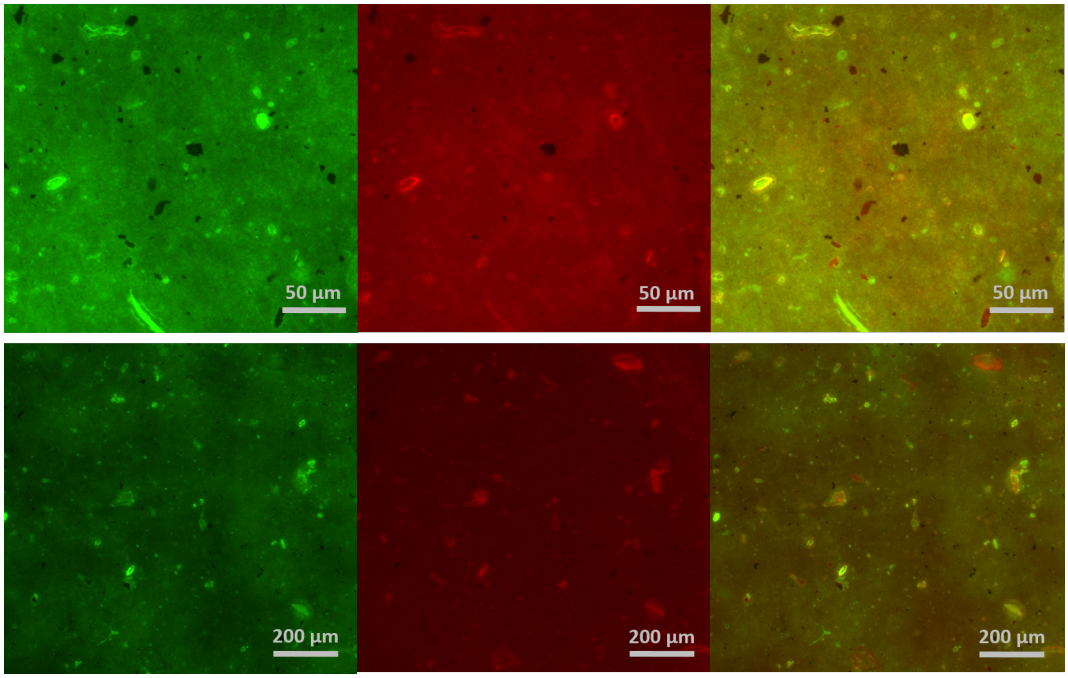

Figure 4.35 – Fluorescence microscopy images of the green channel, the red channel and the combination of both for the double mat.

and red nanotubes. By looking at the cross-section of the mat on figure 4.37, two layers can be observed: a green layer in the lower part of the mat which is in contact with the PET substrate and a red layer in the upper part. However it can be seen that these two layers strongly interpenetrate and do not have a sharp internal interface. This interpenetration can be caused by the diffusion of the nanotubes, but also by partial mixing in suspension during the build-up. Indeed, during the filtration, the PET substrate and the mat which is forming are always immersed in solvent. Therefore, when the second solution is poured over the filtration system, inducing some turbulence, partial mixing of the previously deposited nanotubes can occur with the new ones.

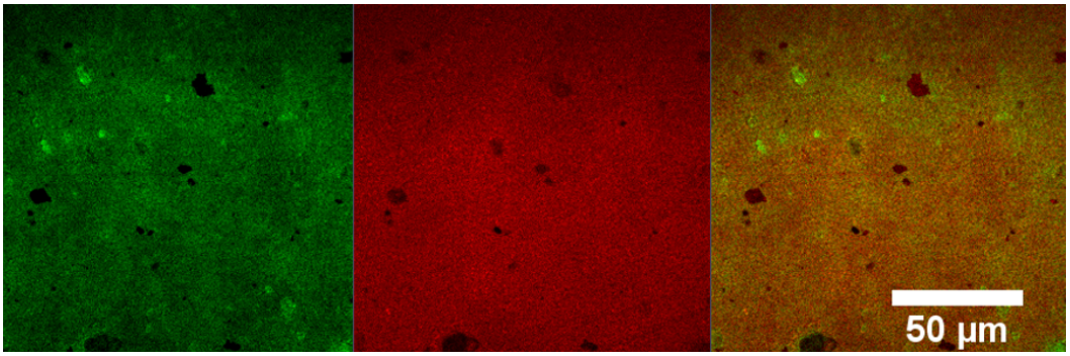

Figure 4.36 – CLSM images of the green channel, the red channel and the combination of both for a plane in the middle of the double mat.

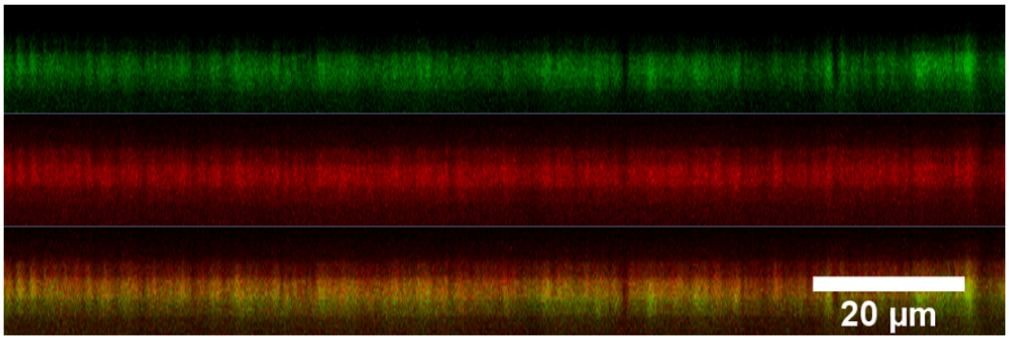

Figure 4.37 – CLSM images of the green channel, the red channel and the combination of both for a cross-section of the double mat (spacing of 0.37 μm between the planes of the stack).

4.3 PAH/PAA system

Another polyelectrolyte combination which is frequently studied, and furthermore easily functionalizable, is PAH/PAA which are two weak polyelectrolytes.[13, 25] The growth of PAH/PAA multilayers in PC nanopores of 300 nm was studied by porometry measurements in the same conditions as for PAH/PSS multilayers, that is, with a decrusting step every third bilayer. The evolution of the pore diameter according to the number of bilayers is compared with the evolution of the PAH/PSS system in figure 4.38 for 3, 6 and 9 bilayers. These results indicate that, by comparison, the alternate adsorption of PAH and PAA is very weak: the wall thickness after the deposition of 9 bilayers is 35.5 nm instead of 80.5 nm for the PAH/PSS system in the same conditions. That means that the growth laws depend heavily on the nature of the polyelectrolytes (as confirmed by [3]). So the results previously obtained for the PAH/PSS system can not be directly transposed for other material combinations.

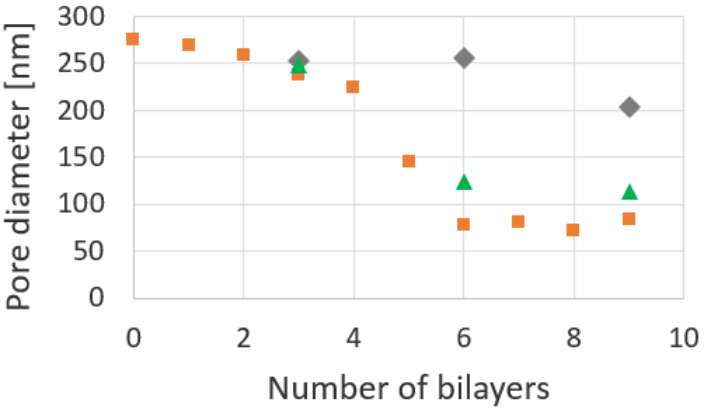

Figure 4.38 – Evolution of the pore diameters estimated by gas-flow porometry as a function of the number of bilayers for PAH/PSS nanotubes decrusted after each bilayer (orange squares) or decrusted after 3, 6 and 9 bilayers (green triangles) and for PAH/PAA nanotubes decrusted every third bilayer (grey diamonds).

The nanotubes from the three previous samples were then released and imaged by SEM in figure 4.39. The image for 3 bilayers shows only small clusters of polyelectrolytes and fragments of nanotubes. As explained by Arys et al.[3], the growth of the PEM begins by the formation of islands on the template pore walls due to the polyelectrolyte adsorption around the imperfections. Then by increasing the number of deposition cycles, islands merge together and form a continuous layer. In our case, the deposition of 3 bilayers is insufficient to ensure that the islands merge together. Therefore only small fragments are observed. By increasing the number of bilayers to 6, nanotube fragments become longer but their length is far from 25 μm as it should be. That means that either the PEM growth is still not linear after the deposition of 6 bilayers, i.e., all the islands did not merge, or the nanotubes are mechanically unstable and break during the releasing and filtration steps because of too thin walls. After the deposition of 9 bilayers, nanotubes are longer and more rigid but their length is still much smaller than 25 μm. In order to strengthen the nanotubes, two options are available, either increasing the number of bilayers or cross-linking the PEM. A post-crosslinking with sulfo-NHS and EDC was applied for nanotubes with 6 bilayers (see section 2.4.4 for the reaction scheme). The resulting nanotubes are imaged in figure 4.39 **d**. Nanotubes are much more rigid; this cross-linking mechanism is thus very effective to strengthen PAH/PAA PEM. The length of the cross-linked nanotubes is nevertheless still too small so the ideal option would be to increase the number of deposition cycles and to perform a cross-linking.

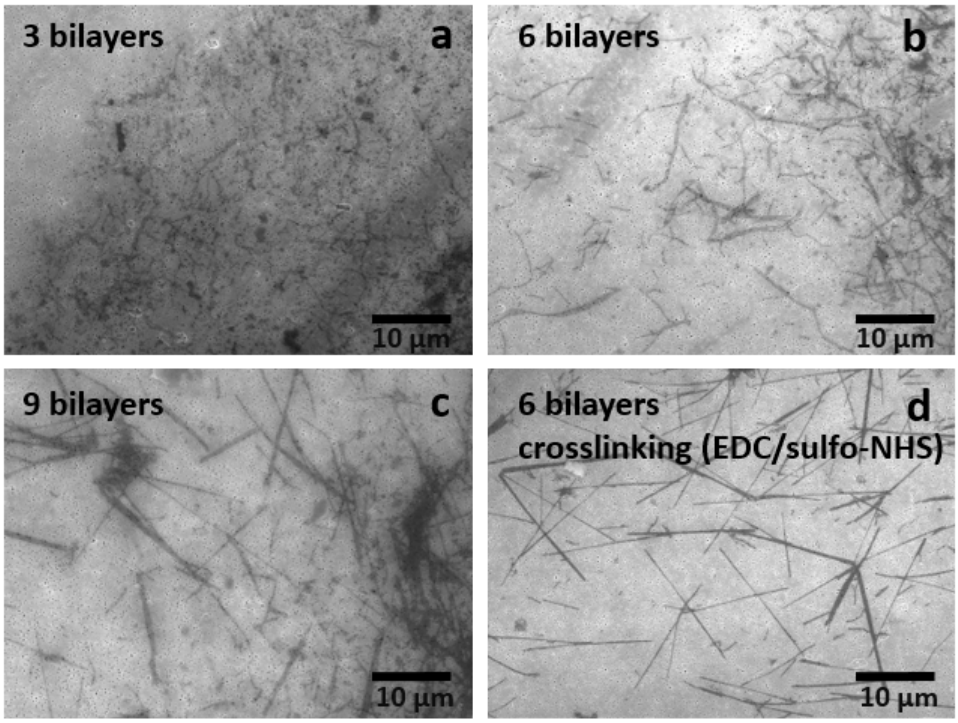

Figure 4.39 – SEM images of PAH/PAA nanotubes with 3, 6 and 9 bilayers without cross-linking and PAH/PAA nanotubes with 6 bilayers and cross-linking.

A mat was prepared in the same conditions as for PAH/PSS system, from nanotubes with 6 bilayers decrusted after the deposition of 3 and 6 bilayers. But the formation of the mat was not possible as observed by optical microscopy in figure 4.40. However these images provide new information about the mat build-up. Indeed it can be seen that the nanotube deposition begins in the hollows created by the attraction of the PET membrane in the filter holes under the effect of the pump. Once these hollows are covered the nanotube deposition widens between them. Therefore the shape of the filter has an influence on the mat build-up.

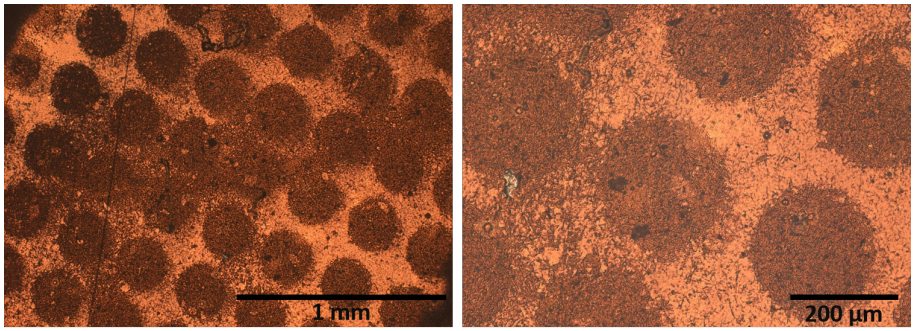

Figure 4.40 – Optical microscopy images of an early mat of PAH/PAA nanotubes.

Chapter 5

Conclusion

The general aim of this study was to improve the knowledge of the building process of mats made of LbL nanotubes and its control parameters. Before dealing with the characterization of the mats, an important part of this project was about the characterization of nanotubes in order to choose the optimal conditions to assemble nanotubes that will be used to form the mats. Therefore the PEM growth, the morphology and the rigidity of the nanotubes were studied as a function of the number of bilayers, the decrusting frequency and the nanotube diameter. For this study, we first chose to focus on PAH/PSS nanotubes.

For nanotubes with an outer diameter of 300 nm, porometry measurements have shown that it was not necessary to adsorb more than 6 bilayers. After 6 deposition cycles, the PEM growth enters a second regime where the diffusion of polyelectrolyte chains is limiting and the thickness increment per bilayer becomes very low. Furthermore the decrusting of the PC template is necessary to limit the clogging of the nanotubes but a decrusting after each bilayer is not absolutely necessary since the decrusting every third bilayer produce nanotubes with similar wall thicknesses. When the diameter of the template pores varies, the growth differs too. For a diameter of 100 nm, the PEM growth reaches faster the second regime while for a diameter of 800 nm, the PEM does not yet reach the second regime after the deposition of 9 bilayers. The largest diameter has the same behavior as a flat substrate for which the confinement does not have any effect and the thickness increment per bilayer is smaller.

SEM and AFM analyses have revealed the effect of the decrusting on the PC template and shown that a lot of pores were clogged with an area density of clogged pores increasing with the number of bilayers. After the dissolution of the PC template and the release of the nanotubes, the nanotube length is slightly shorter than the template thickness probably due to an effect of the decrusting; and the nanotube outer diameter is much smaller than the template pore diameter because of the collapse of the nanotube walls. The study of the nanotube rigidity as a function of the number of bilayers, for nanotubes with an outer diameter of 300 nm, has shown that the thickness increment for each extra bilayer makes the nanotubes more rigid. For a constant number of bilayers, nanotubes with a larger outer diameter are more rigid.

On the basis of all the results for individual nanotubes, we chose to build mats from nanotubes with 6 bilayers which are decrusted every third bilayer. As observed by SEM and AFM, the mats are networks of very entwined fibers where the nanotubes are still clearly observable although some parts seem to have merged. When the mat is formed from nanotubes with a larger number of bilayers, nanotubes in the mat are more rigid as it was observed for individual nanotubes. The morphology of the mats was also compared between dry and humid environments but the swelling was too small to be detected by the AFM analysis.

By studying the morphology of the mat as a function of the nanotube area density, we have demonstrated that there was a threshold density, between $5.66 * 10^8$ and $1.13 * 10^9$ cm^{-2}, in order to form a continuous mat. Furthermore, once the substrate is entirely covered by the nanotubes, the mat build-up presents an intermediary phase where the nanotubes organize themselves in islets and then additional nanotubes fill the less dense areas. The nanotube sedimentation is thus not homogeneous over the whole surface and the thickness does not increase linearly with the number of nanotubes. This was also confirmed by the measurement of the full width at maximum height obtained from CLSM cross-sections. Finally the AFM analysis has shown that the addition of nanotubes does not modify the surface roughness and thus the surface porosity. The same study was performed to understand the influence of the nanotube diameter and has shown that the larger the diameter is, the thicker the corresponding mat is and the rougher the mat surface is.

The Young's modulus of a mat was measured by AFM in the force spectroscopy mode with sensors with integrated colloidal particles. With a sensor cantilever softer than the contact stiffness, the average Young's modulus of the mat was 116 MPa which is close to the Young's modulus of PAH/PSS PEM in the literature (200-400 MPa). With a sensor having a stiffness constant closer to the contact stiffness, the Young's modulus could not be measured.

We have also shown that it was possible to build a multilayered mat by the repetition of filtration steps. PAH/PSS nanotubes which were labeled with PAH-FITC and PAH-RITC were alternately filtered and formed two continuous and homogeneous layers. However these two layers strongly interpenetrate each other and do not have a sharp interface.

Finally, a small part of the analysis was repeated with two weak polyelectrolytes, PAH and PAA. By comparison with PAH/PSS nanotubes, the growth of PAH/PAA nanotubes is very slow. So the growth laws depend heavily on the nature of the polyelectrolyte and the results obtained for the PAH/PSS system can not be transposed for all polyelectrolyte combinations. To strengthen PAH/PAA nanotubes which are still too fragile even after the deposition of 9 bilayers, a post-crosslinking with sulfo-NHS and EDC is effective.

This study provides thus a first analysis for the build-up of mats of LbL nanotubes. There remain, however, a lot of unanswered questions and options to be explored to have a deeper understanding of the process. There are for example some unexplored

processing parameters such as pH and ionic strength of the aqueous solutions used for nanotube production or molar mass of the polyelectrolyte. Among the discussed ways that should be deepened, we could analyze the mat build-up with larger nanotube area densities than $2.26 * 10^9$ cm^{-2} to check whether the growth with clusters is repeated for larger densities. About the thickness of the mat, it was approximated by CLSM and optical microscopy but accurate measurements were so far not possible. In this context, it could be worth performing profilometry on the mat. The study of multilayered mats should also be more investigated by studying the influence of the build-up process on mat interfaces. For example, it would be worth analyzing the mat interface if some air is filtered between the filtration of the two single mats. Moreover the analysis could also be repeated with the successive filtration of three or four single mats.

In addition, characterization of the mat's physical properties was only briefly discussed. The study of the Young's modulus should be more deeply investigated by repeating AFM force spectroscopies on several samples with sensors of varying stiffness constants. If measured values still vary too much, it would be interesting to use sensors with larger colloidal particles to indent a larger area and limit the influence of the inhomogeneities of the mat. As a second step, the Young'modulus should be characterized by some varying parameters such as the number of nanotubes per unit surface. Moreover, mechanical properties should also be assessed on a larger scale by traction experiments on the mats.

It is in this context that Prof. Alain Jonas and Prof. Karine Glinel will work in Robert Langer's lab (MIT, USA) next year to focus on the understanding of the process and the exploring of the application range of this process. Among the numerous possible applications of the mats, mats could have a function of scaffold to control a crystallization process or serve as biocompatible porous electrodes or scaffold for cell growth. Multilayered mats could also be used to generate an enzymatic cascade.[1]

Bibliography

[1] A. Jonas. Multilayered mats of layer-by-layer-assembled soft nanotubes: From biocatalytic cascades to biomineralization matrices and conducting cell culture substrates. Project submitted for evaluation by the jury of the Marcel de Merre Prize, 2015-2017 edition.

[2] R. Dersch, M. Steinhart, U. Boudriot, A. Greiner, J. H. Wendorff. Nanoprocessing of polymers: applications in medicine, sensors, catalysis, photonics. *Polymers for Advanced Technologies* **2005**, 16, 276-282.

[3] X. Arys, A. M. Jonas, A. Laschewsky, R. Legras, F. Mallwitz. Layered polyelectrolyte assemblies. In Supramolecular Polymers, 2nd edition, A. Ciferri, Ed. CRC: Boca Raton, **2005**; pp.651-710.

[4] C. J. Roy, C. Dupont-Gillain, S. Demoustier-Champagne, A. M. Jonas, J. Landoulsi. Growth mechanism of confined polyelectrolyte multilayers in nanoporous. *Langmuir* **2010**, 26, 3350-3355.

[5] S. Saghazadeh, S. Zhang, D. Lefèvre, A. Le Beulze, A. M. Jonas, S. Demoustier-Champagne. Universal method to transfer membrane-templated nano-objects to aqueous solutions. *Langmuir* **2015**, 31, 7264-7273.

[6] C. Roy. Membrane-templated nanotubes as potential candidates for drug delivery applications. PhD thesis, Université catholique de Louvain, **2012**.

[7] It4ip Ion Track Technology. `http://www.it4ip.be/` Accessed 9 May 2016.

[8] G. Decher, J. D. Hong. Buildup of ultrathin multilayer films by a self-assembly process, 1 consecutive adsorption of anionic and cationic bipolar amphiphiles on charged surfaces. *Makromolekulare Chemie, Macromolecular Symposia* **1991**, 46, 321-327.

[9] H. Alem, F. Blondeau, K. Glinel, S. Demoustier-Champagne, A. M. Jonas. Layer-by-layer assembly of polyelectrolytes in nanopores. *Macromolecules* **2007**, 40, 3366-3372.

[10] Q. He, Y. Cui, S. Ai, Y. Tian, J. Li. Self-assembly of composite nanotubes and their applications. *Current Opinion in Colloid & Interface Science* **2009**, 14, 115-125.

[11] S. Hou, C. C. Harrell, L. Trofin, P. Kohli, C. R. Martin. Layer-by-layer nanotube template synthesis. *Journal of the American Chemical Society* **2004**, 126, 5674-5675.

[12] M. Schönhoff. Layered polyelectrolyte complexes: physics of formation and molecular properties. *Journal of Physics: Condensed Matter* **2003**, 15, 1781-1808.

[13] P. Bieker, M. Schönhoff. Linear and exponenetial growth regimes of multilayers of weak polyelectrolytes in dependence on pH. *Macromolecules* **2010**, 43, 5052-5059.

[14] G. Decher. Fuzzy nanoassemblies: toward layered polymeric multicomposites. *Science* **1997**, 277, 1232-137.

[15] Q. An, Y. Zhou, Y. Zhang, Y. Zhang, F. Shi. A facile method for the fabrication of covalently linked PAH/PSS layer-by-layer films. *RSC Advances* **2014**, 4, 5683-5688.

[16] O. Azzaroni, K. H. A. Lau. Layer-by-layer assemblies in nanoporous templates: nano-organized design and applications of soft nanotechnology. *Soft Matter* **2011**, 7, 8709-8724.

[17] ThermoFisher Scientific. `https://www.thermofisher.com/order/catalog/product/22980` Accessed 9 May 2016.

[18] P. Bertrand, A. Jonas, A. Laschewsky, R. Legras. Ultrathin polymer coatings by complexation of polyelectrolytes at interfaces: suitable materials, structure and properties. *Macromolecular Rapid Communications* **2000**, 21, 319-348.

[19] D. Lee, A. J. Nolte, A. L. Kunz, M. F. Rubner, R. E. Cohen. pH-induced hysteretic gating of track-etched polycarbonate membranes: swelling/deswelling behavior of polyelectrolyte multilayers in confined geometry. *Journal of the American Chemical Society* **2006**, 128, 8521-8529.

[20] Y. Cho, C. Lee, J. Hong. Pore size effect on the formation of polymer nanotubular strauctures within nanoporous templates. *Colloids and Surfaces A: Physicochem. Eng. Aspects* **2014**, 443, 195-200.

[21] Z. Feldötö, I. Varga, E. Blomberg. Influence of salt and rinsing protocol on the structure of PAH/PSS polyelectrolyte multilayers. *Langmuir* **2010**, 26, 17048-17057.

[22] M. Lösche, J. Schmitt, G. Decher, W. G. Bouwman, K. Kjaer. Detailed structure of molecularly thin polyelectrolyte multilayer films on solid substrates as revealed by neutron reflectrometry. *Macromolecules* **1998**, 31, 8893-8906.

[23] R. Kügler, J. Schmitt, W. Knoll. The swelling behavior of polyelectrolyte multilayers in air of different relative humidity and in water. *Macromolecular Chemystry and Physics* **2002**, 203, 413-419.

[24] N. Elsner, F. Dubreuil, R. Weinkamer, M. Wasicek, F.D. Fischer, A. Fery. Mechanical properties of freestanding polyelectrolyte capsules: a quantitative approach based on shell theory. *Progress in Colloid and Polymer Science* **2006**, 132, 117-123.

[25] K. Chia, M. F. Rubner, R. E. Cohen. pH-responsive reversibly swellable nanotube arrays. *Langmuir* **2009**, 25, 14044-14052.

[26] S. A. Dougherty, D. Zhang, J. Liang. Fabrication of protein nanotubes using template-assisted electrostatic layer-by-layer methods. *Langmuir* **2009**, 25, 13232-13237.

[27] D. M. Dotzauer, J. Dai, L. Sun, M. L. Bruening. Catalytic membranes prepared using layer-by-layer adsorption of polyelectrolyte/metal nanoparticle films in porous supports. *Nano Letters* **2006**, 6, 2268-2272.

[28] S. Zhang, S. Demoustier-Champagne, A. M. Jonas. Quantitative collection and enzymatic activity of glucose oxidase nanotubes fabricated by templated layer-by-layer assembly. *Biomacromolecules* **2015**, 16, 2382-2393.

[29] R. Balamurugan, S. Sundarajan, S. Ramakrishna. Recent trends in nanofibrous membranes and their suitability for air and water filtration. *Membranes* **2011**, 1, 232-248.

[30] Z. Xu, X. Huang, L. Wan. Membrane with biocatalytic surface. In Surface Engineering of Polymer Membranes. Ed. Zhejiang University Press: Hangzou, Springer-Verlag GmbH Berlin Heidelberg, **2009**; pp.262-305.

[31] Wikipédia. Persistence length. `https://en.wikipedia.org/wiki/Persistence_length` Accessed 9 May 2016.

[32] Atomic Force Microscope Cantilevers (Calibration method of Sader) University of Melbourne. Department of Mathematics & Statistics. `www.ampc.ms.unimelb.edu.au/afm/calibration.html` Accessed 9 May 2016.

[33] B. Nysten. LMAPR2631 Surface analysis part II: scanning probe microscopies. Université catholique de Louvain **2016**.

[34] O. I. Vinogradova, D. Andrienko, V. V. Lulevich, S. Nordschild, G. B. Sukhorukov. Young's modulus of polyelectrolyte multilayers from microcapsule swelling. *Macromolecules* **2004**, 37, 1113-1117.

[35] D. Li, M. W. Frey, Y. L. Joo. Characterization of nanofibrous membranes with capillary flow porometry. *Journal of Membrane Science* **2006**, 286, 104-114.

Rue Archimède, 1 bte L6.11.01, 1348 Louvain-la-Neuve **www.uclouvain.be/epl**